④

GL-TR-89-0329

AD-A219 358

SEISMIC WAVE PROPAGATION, ATTENUATION AND SCATTERING OVER REGIONAL DISTANCES.

M. Nafi Toksöz
Ari Ben-Menahem
Edmond E. Charrette
Anton M. Dainty
Richard L. Gibson, Jr.

Earth Resources Laboratory
Department of Earth, Atmospheric, and
  Planetary Sciences
Massachusetts Institute of Technology
Cambridge, Massachusetts 02139

11 December 1989

Final Report
28 July 1988—27 July 1989

APPROVED FOR PUBLIC RELEASE; DISTRIBUTION UNLIMITED

90 03 20 124

This technical report has been reviewed and is approved for publication.

JAMES F. LEWKOWICZ
Contract Manager
Solid Earth Geophysics Branch
Earth Sciences Division

JAMES F. LEWKOWICZ
Branch Chief
Solid Earth Geophysics Branch
Earth Sciences Division

FOR THE COMMANDER

DONALD H. ECKHARDT, Director
Earth Sciences Division

REPORT DOCUMENTATION PAGE

1a REPORT SECURITY CLASSIFICATION unclassified	1b RESTRICTIVE MARKINGS
2a SECURITY CLASSIFICATION AUTHORITY	3 DISTRIBUTION/AVAILABILITY OF REPORT
2b DECLASSIFICATION/DOWNGRADING SCHEDULE	Approved for public release; distribution unlimited
4 PERFORMING ORGANIZATION REPORT NUMBER(S)	5 MONITORING ORGANIZATION REPORT NUMBER(S) GL-TR-89-0329

6a NAME OF PERFORMING ORGANIZATION Earth Resources Laboratory, Dept. of Earth, Atmospheric, and Planetary Sciences	6b OFFICE SYMBOL (If applicable)	7a NAME OF MONITORING ORGANIZATION Geophysics Laboratory
6c. ADDRESS (City, State, and ZIP Code) Massachusetts Institute of Technology Cambridge, MA 02139		7b ADDRESS (City, State, and ZIP Code) Hanscom AFB, MA 01731-5000

8a. NAME OF FUNDING/SPONSORING ORGANIZATION Defense Advanced Research Projects Agency	8b OFFICE SYMBOL (If applicable) NMRO	9 PROCUREMENT INSTRUMENT IDENTIFICATION NUMBER F19628-88-K-0036

8c. ADDRESS (City, State, and ZIP Code) 1400 Wilson Blvd. Arlington, VA 22209-2308	10 SOURCE OF FUNDING NUMBERS			
	PROGRAM ELEMENT NO	PROJECT NO	TASK NO	WORK UNIT ACCESSION NO
	62714E	7A10	DA	CM

11 TITLE (Include Security Classification)

Seismic Wave Propagation, Attenuation and Scattering Over Regional Distances

12 PERSONAL AUTHOR(S)

M.N. Toksöz, A. Ben-Menahem, E.E. Charrette, A.M. Dainty, R.L. Gibson, Jr.

13a. TYPE OF REPORT Final	13b. TIME COVERED FROM 7/28/88 TO 7/27/89	14 DATE OF REPORT (Year, Month, Day) 89 12 11	15 PAGE COUNT 98

16 SUPPLEMENTARY NOTATION

17 COSATI CODES			18 SUBJECT TERMS (Continue on reverse if necessary and identify by block number)
FIELD	GROUP	SUB-GROUP	coherency; scattering in random media; finite-difference modelling; scattering from anisotropic inclusions

19 ABSTRACT (Continue on reverse if necessary and identify by block number)

The objective of this project was to conduct basic research on the propagation of seismic energy at regional (100-1000 km) distances for purposes of monitoring underground nuclear explosions. The problems studied were the coherency of the seismic S phases, especially Lg, and the implications in terms of the scattering properties of the earth medium; and scattering from anisotropic inclusions. This Final Report consists of preprints of two papers on these subjects. The first concerns the measurement of coherency of the Sn/Lg phases at distances of 200–400 km for quarry blasts recorded at the Fennoscandian arrays ARCESS, FINESA and NORESS, and its interpretation. The measurements indicate wavelength scaling of the spatial coherency, i.e., scaling according to the scale of the wave only, in the frequency band 1–10 Hz; the wavelength range is 0.4–2 km. This suggests there is no medium scale in this size range. Numerical experiments with randomized time series demonstrate that spatial coherency is mainly controlled by phase (travel time) variations. Preliminary work with finite difference modelling of these regional phases shows that crustal models with random velocity variations have the potential to explain the observations.

20. DISTRIBUTION/AVAILABILITY OF ABSTRACT ☒ UNCLASSIFIED/UNLIMITED ☐ SAME AS RPT ☐ DTIC USERS	21 ABSTRACT SECURITY CLASSIFICATION Unclassified
22a. NAME OF RESPONSIBLE INDIVIDUAL James F. Lewkowicz	22b. TELEPHONE (Include Area Code) 617/377-3028 22c. OFFICE SYMBOL GL/LWH

DD FORM 1473, 84 MAR   83 APR edition may be used until exhausted.
All other editions are obsolete.

Unclassified

BLOCK 19: Abstract

In the second paper, the existence of Rayleigh scattering of elastic plane waves by anisotropic homogeneous inclusions is theoretically demonstrated. The case of transverse isotropy is studied in detail. It is shown that an incident longitudinal wave creates radial-longitudinal (P), colatitudinal-shear (SV) and azimuthal-shear waves (SH). Likewise, incident SV and SH waves both generate radial P waves, and SV and SH shear waves. All scattered amplitudes are proportional to the square of the frequency and have radiation pattern signatures of equivalent dipoles, centers of compression and double couples. It is shown that observations of spatial patterns of scattered amplitudes can yield through inversion the elastic constants of the anisotropic inclusion. These results may help explain on a theoretical basis the observed short-period SH and SV waves from underground explosions at teleseismic distances.

Table of Contents

iii

List of Contributing Scientists

M. Nafi Toksöz, Professor of Geophysics, Massachusetts Institute of Technology

Ari Ben-Menahem, Visiting Scientist, Massachusetts Institute of Technology [a]

Anton M. Dainty, Visiting Scientist, Massachusetts Institute of Technology

Edmond E. Charrette, Graduate Research Assistant, Massachusetts Institute of Technology

Richard L. Gibson, Jr., Graduate Research Assistant, Massachusetts Institute of Technology

---

[a] Also NRC Fellow, Earth Sciences Division, Geophysics Laboratory, Air Force Systems Command.

List of Previous and Related Contracts

Bibliography of Publications Totally or Partially Sponsored by the Contract

Toksöz, M.N., E.E. Charrette and A.M. Dainty (1989). Variability of ground motion at Fennoscandian arrays. *Papers Presented at 11th Ann. DARPA/AFGL Seismic Res. Symp.*, 290-300.

Dainty, A.M., E.E. Charrette and M.N. Toksöz (1989). Coherency of ground motion and scattering. *25th General Assembly IASPEI, August 1989, Istanbul, Turkey, Abstracts*, p. 488.

Ben-Menahem, A., and R.L. Gibson, Jr. (1989). Scattering of elastic waves by localized anisotropic inclusions. *J. Acous. Soc. Am.*, in press.

Toksöz, M.N., A.M. Dainty and E.E. Charrette (1989). Coherency of ground motion at regional distances and scattering. *Submitted to* Phys. Earth Planet. Int.

COHERENCY OF GROUND MOTION AT REGIONAL DISTANCES AND SCATTERING

M. NAFI TOKSÖZ, ANTON M. DAINTY AND EDMOND E. CHARRETTE

EARTH RESOURCES LABORATORY

DEPARTMENT OF EARTH, ATMOSPHERIC, AND PLANETARY SCIENCES

MASSACHUSETTS INSTITUTE OF TECHNOLOGY

CAMBRIDGE MA 02139

1

ABSTRACT

In the absence of local scattering the ground motion due to major phases at an array should be perfectly coherent between different seismometers. We have studied the coherency of ground motion for regional phases such as Lg as a function of frequency and spatial separation for the NORESS, ARCESS and FINESA arrays. Events examined are quarry blasts at a distance of 200-400 km from the array. Coherency was estimated for 10-25 s windows containing the phase and with the array seismograms time shifted to remove the average effect of propagation across the array. In the 1-10 Hz range coherency decreases with increasing spatial separation. The decrease is faster for higher frequencies, but if the separation is scaled to the wavelength then the decay curves are similar and indicate that coherency decreases to less than 0.5 within about a wavelength. To study this problem we have simulated synthetic seismograms by two methods. Finite difference calculations have been made for a source below a layer over a half space to produce seismograms for an array at the top of the layer. The layer and the half space contain random velocity variations and the layer— half space interface is randomly rough. Models using self-similar autocorrelations for the velocity and interface perturbations reproduce the major features of the observed coherency relations. Synthetic seismograms have also been constructed by taking an observed trace and producing new traces by successively randomly perturbing the Fourier amplitude and/or phase. Perturbations of phase (or equivalently travel time) have a much greater effect on coherency than perturbations of the amplitude.

2

INTRODUCTION

At regional distances (100–2000 km) seismic energy from shallow events travels through the lithosphere. While traditional layered models, including large scale lateral heterogeneity, have succeeded in explaining travel times and the gross amplitudes of regional phases, it is clear that scattering has an important effect. Three effects are notable. One is the presence of coda, scattered energy arriving at times that cannot be explained by layered structures (Aki and Chouet, 1975; Herrmann, 1980). A second is attenuation due to scattering (Dainty, 1981, 1984; Wu, 1982; Toksöz *et al.*, 1989). Both of these effects are primarily controlled by backscattering. The third effect is the incoherence of regional seismic phases even at closely spaced stations, often called fluctuations. This effect is controlled by forward scattering (Chernov, 1960). In this paper we will examine this effect on regional seismograms. While some work has been done on regional phases such as Lg (Der *et al.*, 1984; Ingate *et al.*, 1985), the effect has been studied extensively for teleseismic arrivals (Aki, 1973; Capon, 1974; Flatté and Wu, 1988), and some work has also been carried out in the field of strong motion studies (Farjoodi *et al.*, 1985; Loh, 1985; Harichandran and Vanmarcke, 1986; Toksöz *et al.*, 1989). Our goal is to measure the coherence of the regional phase Lg in Fennoscandia and offer a preliminary interpretation in terms of the features of the wavefield and the earth that might be causing it. All of the areas studied have Precambrian or Paleozoic crystalline rock exposed at the surface.

Regional arrays such as NORESS (Bungum *et al.*, 1985), FINESA (Korhonen *et al.*,

3

1987) and ARCESS (Mykkeltveit *et al.*, 1987) provide powerful tools to examine the effect of scattering on seismograms. In previous investigations at NORESS (Dainty, 1985, 1989; Dainty and Harris, 1989) we have looked at coda, which consists of scattered energy often deviating at large angles from the direct arrivals. In such a situation frequency-wavenumber analysis has proven to be useful because the arrays can resolve the differences in angle clearly. When the effect of scattering on direct phases such as Lg is considered, however, this method does not produce useful results because the angle of deviation of the (forward) scattered energy is not resolvable by the array.

Previous work on this problem has used the fluctuations of amplitude and phase (arrival time) of teleseismic P at the LASA (Aki, 1973; Capon, 1974) and NORSAR (Capon and Berteussen, 1974; Flatté and Wu, 1988) arrays to estimate statistical parameters of P velocity perturbations in the lithosphere below the arrays. Since teleseismic P is an isolated (in time) arrival that travels near vertically through the lithosphere the effects of horizontally layered structure and scattering are effectively decoupled and analytic infinite random medium theories may be used. These theories predict that forward scattering will predominate, that it is controlled by the velocity fluctuations (Wu and Aki, 1985), and that acoustic theory may be used. The measured quantities are statistical variables of the wavefield such as variances of the log amplitude and phase, and spatial and angular correlations and covariances of these quantities. In the most recent work Flatté and Wu (1988) treat 1–3 Hz waves at the NORSAR array (diameter 110 km, minimum element spacing 3 km). They

find the data can be explained by two overlapping layers with power law (i.e., scale free) spectra of velocity fluctuations. The upper layer, from 0–200 km, has a flat power spectrum. while the lower from 15–250 km has a power spectrum that varies as k^{-4} ("self-similar"). where k is the wavenumber of the spectrum of the fluctuations. The RMS size of the velocity fluctuations is a few %, similar to other investigations.

One result of some importance from this work is the short distance (~ 10 km) over which arrivals lose coherence. For regional phases at higher frequencies even more rapid loss of coherence might be expected. This indicates that information from dense arrays of small aperture is needed, and since travel time and amplitude fluctuations will be smaller new analysis methods are desirable. Accordingly, to evaluate the effect of scattering on direct phases the spatial coherency has been calculated using methods developed for analysis of strong motion array records (Vanmarcke, 1983). The coherency is a frequency domain equivalent of the correlation function used by Bungum *et al.* (1985) and Ingate *et al.* (1985). Interpretation of the coherency for regional phases presents a challange, however, because of the horizontal propagation of energy in a horizontally layered structure (the crust): under such circumstances the effects of scattering and propagation are not decoupled (e.g., Kennett, 1986). Two methods are used to help solve this problem. One is a purely statistical method of constructing a more or less "random" set of seismograms by starting with an observed trace and producing new traces by randomly perturbing the Fourier amplitude and/or phase. While this does not give any information about the earth, it allows us to see what features

5

of the wavefield are affecting the coherency. The other method is to compute theoretical seismograms for layered scattering media by finite differences, calculate the coherency and compare it with observations. However, due to computational limitations it is not possible to make a full comparison.

METHODS—DATA ANALYSIS AND THEORY

Computing Spatial Coherency

The lagged coherency is

$$C(x,\omega) = \frac{S_{ij}(x,\omega)}{[S_{ii}(\omega)S_{jj}(\omega)]^{1/2}} \tag{1}$$

where S_{ij} is the cross spectrum of seismograms $s(x_i)$, $s(x_j)$, lagged to remove time shifts due to travelling wave propagation; the separation $x = x_i - x_j$. S_{ii} and S_{jj} are the autospectra of the two seismograms. To compute the coherency we used methods due to Jenkins and Watts (1969) and Vanmarcke (1983). These authors demonstrate that gross time shifts due to wave propagation across the array must be removed before accurate estimates of the coherency can be made. Initial estimates of the lag times were found by using frequency-wavenumber analysis (Capon, 1969) to estimate the velocity and azimuth of the mean plane wave and then calculating the lags. The cross correlation and autocorrelations of a shifted pair of seismograms are then windowed with a Hamming window of width 0.5–1 s and the cross spectrum, autospectra and coherency computed. The purpose of the Hamming windowing

was to provide frequency smoothing to control bias at low coherencies (Jenkins and Watts, 1969). To see the necessity for this note that if no frequency smoothing is applied, it may be shown that C in (1) is identically unity, i.e., two perfect harmonic components from a finite length signal are perfectly coherent. This bias becomes more troublesome as the coherency decreases. We have demanded that the frequency-bandwidth product be at least 10; this allows successful calculation of coherencies of magnitude 0.4-0.5 and higher.

Lengths of data in the original seismograms are 3-25 s. This procedure is then repeated for every possible pair of seismograms in the array. In the plots of coherency (i.e., the absolute value of the coherency) and phase lag (the value of the phase of the calculated coherency, a complex quantity), each cross is such a determination. These determinations are then averaged over an appropriate spatial interval and the standard deviations found, using the Fisher Z-transform (Jenkins and Watts, 1969) for the coherency; these averages are plotted as points with error bars. Finally, the phase lag is checked to ensure that the averaged values are close to zero (within $\pm\pi/2$); if they are not a new value of the velocity and/or azimuth is tried until they are. We do not adjust the lags other than through the velocity and azimuth—on occasion, there is residual structure in the phase lags indicating that the signal is not a simple plane wave.

Finite Difference Modelling in Highly Heterogenous Media

To help analyse the results in terms of scattering of seismic waves in media with randomly varying velocity fields, we use the finite difference method for producing synthetic seismograms. Coherency can then be calculated for a set of synthetic seismograms from a model with specified statistics and compared with the observations. The technique is attractive because it produces a full solution to the elastic wave equation, thus all direct, converted, diffracted and guided waves are accurately modelled. Also, unlike various high frequency approximations, there is no limitation on the ratio of scatterer size to wavelength. This property is essential when modelling waves in media with self-similar velocity fields.

The equations of motion for wave propagation in a two-dimensional, elastic, isotropic media can be written in terms of horizontal (u) and vertical (w) particle displacements.

$$\rho\frac{\partial^2 u}{\partial t^2} = \frac{\partial}{\partial x}\left[(\lambda + 2\mu)\frac{\partial u}{\partial x} + \lambda\frac{\partial w}{\partial z}\right] + \frac{\partial}{\partial z}\left[\mu(\frac{\partial u}{\partial z} + \frac{\partial w}{\partial x})\right] + F_x$$

$$(2)$$

$$\rho\frac{\partial^2 w}{\partial t^2} = \frac{\partial}{\partial x}\left[\mu(\frac{\partial u}{\partial z} + \frac{\partial w}{\partial x})\right] + \frac{\partial}{\partial z}\left[(\lambda + 2\mu)\frac{\partial w}{\partial z} + \lambda\frac{\partial u}{\partial x}\right] + F_z.$$

In this formulation the Lamé constants λ and μ and density ρ are freely varying functions of position (x, z), and F is the body force term. Unlike earlier finite difference studies in this area (e.g., Frankel and Clayton, 1986), we use a staggered second order finite difference scheme to solve Equation (2). This method is capable of more accurately modelling rapidly varying media, in part because the effective sampling rate of the velocity field is twice as

8

great as that for a non-staggered grid (Virieux, 1984, 1986). At present we have limited our computations to two-dimensional models.

Constructing Random Velocity Perturbations

Random media can be characterized by three basic quantities, their correlation function (or fluctuation spectrum), their probability distribution, and their standard deviation (or spectral amplitude). There are many different correlation functions which can be used to describe a random medium, but in this presentation we will only be concerned with zeroth order Von Karman functions (Tatarskii, 1961). In two dimensions, the wavenumber domain representation of this class of functions can be written in terms of the correlation length a and the horizontal and vertical wavenumbers k_x and k_z as,

$$P(k_x, k_z) = \frac{a^2}{1 + a^2(k_x{}^2 + k_z{}^2)}.$$ (3)

The outstanding feature of media with this correlation function is the presence of roughness at all length scales. This property is often seen in nature (Mandelbrot, 1977), and is thought to best reflect the random portion of the earth's velocity field (Wu, 1982; Dainty, 1984; Frankel and Clayton, 1986).

Two-dimensional realizations for each of the three material properties, Lamé's parameter, shear modulus, and density, were constructed by inverse Fourier transforming the product of the wavenumber representation of the zeroth order Von Karman function and a random phase term. When transformed back to the space domain, each of the three functions will

have the desired autocorrelation function, zero mean and a Gaussian probability distribution.

OBSERVATIONS AT FENNOSCANDIAN ARRAYS FROM QUARRY BLASTS

To examine the coherency of Lg from regional events data from the three Fennoscandian arrays mentioned previously, ARCESS, FINESA and NORESS, was used. The locations of the arrays are given in Table 1 and Figure 1 shows the configurations. While all three arrays contain three component stations, only vertical components have been used in this study. Further details of the arrays are in the cited references. Results are presented for four events in the distance range 200–400 km; information about these events is summarized in Table 2. All of the events are believed to be quarry blasts either on the basis of location at a known quarry and/or the presence of a strong Rg phase. Time windows for analysis are selected to include not only Lg but also Sn and Sg, if they are present. Any Rg phase, however, was excluded. It was found that the coherency analysis was not sensitive to small shifts of the window.

To illustrate the analysis, we choose the 15 November 1985 event recorded at the FINESA array. Figure 2 shows the array seismograms with the analysis window indicated. In Figure 3 the power spectrum and the frequency-wavenumber diagram for a frequency of 3.6 Hz are presented. Figures 4 and 5 show the absolute value of the coherency and the phase of the coherency of the lagged traces. Figure 5 demonstrates that the averaged phase lags are within

10

$\pm\pi/2$ of zero, as required. Figure 4 illustrates that coherency decays with increasing spatial separation more rapidly at higher frequencies. Figure 6 shows the seismograms at the array center seismometer for the other events, and Figure 7 presents the absolute value of coherency for the event recorded at NORESS, illustrating more clearly the increasingly rapid decline of coherency with separation as frequency increases. In Figures 4, 5 and 7, and throughout this paper, spatial separation is taken as the absolute distance between seismometer pairs without regard to whether the separation vector is oriented along or perpendicular to the azimuth of the wave. We find that there is no apparent difference between these cases, in agreement with work on teleseismic arrivals (Aki, 1973; Capon, 1974) and strong motion (Harichandran and Vanmarcke, 1986). This is contrary to the findings of Der *et al.* (1984), but most of these authors' results are at lower frequencies.

As stated above, coherency declines with increasing separation and declines faster for higher frequencies. We attribute this decline in coherency to scattering. By looking at different frequencies we have examined different wavelengths. In an attempt to gain an integrated look at the data, Figures 8 and 9 plot the spatially averaged coherencies for all events and frequencies analysed against distance in *wavelengths*. Intriguingly, within error limits it appears that the curves of decline of coherency with separation for the different frequencies are all very similar if the separation is scaled to the wavelength. The effect is most dramatic for the event recorded at NORESS. The curves for different events appear to be similar; this may reflect the similarity of site/path heterogeneities for these crystalline

11

rock sites within the Fennoscandian shield. Note that the coherency declines to $\sim$ 0.5 within about one wavelength.

For a preliminary interpretation of these results, we note that in spite of travelling several hundred kilometers through the lithosphere regional seismograms still show distinct phases such as P and Lg, i.e., the effect of scattering is not so strong as to obliterate all features of wave propagation. This suggests the scaling illustrated in Figures 8 and 9 must be a propagation effect and indicates that the heterogenities in the lithosphere must also scale in some manner. This has led us to investigate self-similar models of velocity and density perturbations in the crust as discussed in the next section. The term "self-similar" is here taken to mean having a power law spectrum, at least within a certain range of length scales. For strict self-similarity this range is 0 to ∞, but it is not possible to construct a finite realization for such a case because a power law spectrum will tend to ∞ at one of the limits. Thus the Von Karman function defined in Equation (3) is asymptotically self-similar for short length scales (high wavenumbers) but is not self-similar for length scales longer than the parameter a, which is a length. The appropriate length scales are set by the wavelengths of the waves analysed, which are in the range 0.4-2 km.

THEORETICAL INVESTIGATIONS

Coherency of Randomized Time Series

In interpreting coherency it is of interest to know whether fluctuations in amplitude or phase (travel time) of the seismograms are important. To examine this question randomized time series were constructed, starting with real data, and then analysed as if they were spatially separated seismograms. An example is shown in Figure 10. The top trace is the top trace of Figure 2 within the window shown on Figure 2. To produce the second trace the Fourier transform of the top trace is calculated, randomly perturbed while maintaining its symmetry properties about zero frequency, and transformed back into time. In this case only the phase of the Fourier transform was perturbed; Figure 11 shows the perturbations, which are scaled with frequency so as to model travel time shifts of 0.04 s maximum. The third trace is constructed from the second trace in a similar manner (with a different realization of perturbations) and so on, i.e., a set of "seismograms" that are succesively more unlike the initial seed are produced, just as might be expected for a suite of records at increasing spatial separation. Figure 12 presents coherency at 4 Hz for the time series shown in Figure 10 computed as if successive traces were 200 m apart. The coherency decays with increasing "separation" and is of the same order of magnitude as the observations presented earlier. Numerical experiments such as this have demonstrated that phase perturbations are much more important than amplitude perturbations in controlling coherency.

13

Finite Difference Modelling

While the effort using randomized fields is instructive, it is also clearly not reproducing some features of the data. To give one example, the seismograms in Figure 2 all exhibit the characteristic of a definite "S" arrival at about 29 s. In Figure 10, this corresponds to the peak at 1.8 s on the first trace, which is taken from the top trace of Figure 2, but the other traces do not in general maintain this characteristic. The fundamental difficulty is that the "model" is not physical and thus does not contain the concept of seismic phases, for example. To remedy this we have begun to use finite difference calculations to compute array seismograms which can then be analysed in the same manner as observed seismograms. However, while the finite difference method allows the calculation of complete seismograms in a physical model, computational limitations cause the models that can be realistically considered to be smaller than desirable and the signals to have a narrow frequency range.

The work in finite difference has just begun and so only an example will be presented here. In Figure 13 a two-dimensional model of a layer over a half space with a rough interface and random velocity and density perturbations is shown. For these trial calculations we have limited the size of the model (6.5×25 km) and the frequency content of the seismic signal (1–5 Hz). The average model has a 6 km thick layer of P velocity 6 km/s overlying a substrate with P wave velocity 7 km/s. Poisson's ratio is 0.25. A power spectrum for the fluctuations of the form (3) was used with the parameter $a = 1.5$ km, equal to the wavelength of P waves at the mean frequency of 3 Hz. The RMS velocity fluctuations are 0.15. Synthetic

14

seismograms for the vertical component are shown in Figure 13 with an analysis window for P indicated. P was chosen for analysis because the source is an explosion and the distance travelled is relatively short, about 10 wavelengths. These seismograms were taken for an array between 22 and 24 km distance on the surface of the model and were spaced 125 m apart. The appropriate lagging velocity for these seismograms in this window was found to be 4.5 km/s, slower than the P wave velocity of 6 km/s. This indicates scattering to S.

Figure 14 shows the coherency at the center frequency of 3 Hz for these synthetic seismograms. Noting that the wavelength at 4.5 km/s and 3 Hz is 1.5 km, we see that the results in Figure 14 agree roughly with Figures 4 and 7. A further comparison emphasising the agreement is shown in Figure 15 which presents the synthetic results on a wavelength scaled plot with the observations from the NORESS event. Work with layered media for strong motion modelling (Toksöz et al., 1989) has demonstrated that the velocity perturbations are more important than the rough interface in producing a loss of coherency.

DISCUSSION AND CONCLUSIONS

A crucial issue in research into seismic scattering is the nature of the earth structure causing it. In this investigation we have concentrated on the seismic S phases at regional distances; this limits the investigation to the crust (Lg) or possibly the uppermost mantle (Sn). By choosing locations in the crystalline province of Fennoscandia any effects due to near-surface sedimentary layers has been eliminated. Also, by looking at direct phases we have empha-

15

sized forward scattering as opposed to backscattering. Forward scattering is sensitive to large scale fluctuations and to velocity perturbations. Backscattering is sensitive to smaller scale fluctuations than forward scattering for the same wavelength of the incident wave and to impedance contrasts rather than velocities (Wu and Aki, 1985). Thus the scatterers responsible for the effects seen in this study are not necessarily the same as those responsible for such phenomena as coda and attenuation which are controlled by backscattering.

Our array measurements of coherency in Fennoscandia demonstrate that it declines to ~ 0.5 within about a wavelength. This wavelength scaling is scaling according to the length scale of the wave; there is no sign in the wavelength range examined (0.4–2 km) of a length scale for the medium affecting the results. This is explainable by propagation in a medium with a power law spectrum of medium heterogeneity such as those used by Flatté and Wu (1988) for teleseismic observations. The coherency statistics appear to be isotropic (i.e., they do not depend on direction with respect to the azimuth of the incoming wave), in agreement with observations of teleseismic phases in the same region (Flatté and Wu, 1988) and strong motion observations in Taiwan (Harichandran and Vanmarcke, 1986). We do not observe the distinction between on azimuth and perpendicular to azimuth separations seen at lower frequencies by Der *et al.* (1984).

To assess the causes of the loss of coherency, randomized time series were examined to see what features of the observed wavefield were important. Phase (or travel time) variation was found to be dominant over amplitude variation, reinforcing the importance of velocity

16

perturbations, since they control travel times. Travel time variations of the order of 0.01 sec over 100 m at 4 Hz were found to be sufficient to explain the data.

To provide a satisfactory explanation of the observations, a physical model of the propagation of seismic waves through appropriate earth models which include scatterers is required. In preliminary work, similar effects to those observed have been found in synthetic seismograms calculated for models with rough boundaries and random variations of velocity and density. At present, however, computational limitations have prevented a thorough test. The linear dimensions of the models are too small for direct comparison and they are two-dimensional rather than three-dimensional. Related to the problem of model size is the high value of RMS perturbation that had to be used, 15%, to produce the desired loss of coherency. This is considerably higher than the 1–5% range found in studies of teleseismic data in the same region (Capon and Berteussen, 1974; Flatté and Wu, 1988), although these studies are at somewhat lower frequencies. In addition, we have not yet tested the wavelength dependence of the loss of coherency. Future work will concentrate on this question both by using more powerful computers for the finite difference calculations and by exploring analytical methods such as those of Flatté *et al.* (1979).

ACKNOWLEDGEMENTS

17

REFERENCES

Ahjos, T., Pelkonen, E., Franssila, M., Mustila, L. and Komppa, M., 1986a. Seismic events in northern Europe November-December 1985. Inst. Seis., Univ. Helsinki, Helsinki.

Ahjos, T., Pelkonen, E., Franssila, M. and Komppa, M., 1986b. Seismic events in northern Europe February 1986. Inst. Seis., Univ. Helsinki, Helsinki.

Aki, K., 1973. Scattering of P waves under the Montana Lasa. J. Geophys. Res., 78: 1334–1346.

Aki, K. and Chouet, B., 1975. Origin of coda waves: source, attenuation and scattering effects. J. Geophys. Res., 80: 3322–3342.

Bungum, H., Mykkeltveit, S. and Kværna, T., 1985. Seismic noise in Fennoscandia, with emphasis on high frequencies. Bull. Seis. Soc. Am., 75: 1489–1513.

Capon, J., 1969. High-resolution frequency-wavenumber spectrum analysis. Proc. IEEE, 57: 1408–1418.

Capon, J., 1974. Characterization of crust and upper mantle structure under Lasa as a random medium. Bull. Seis. Soc. Am., 64: 235–266.

Capon, J. and Berteussen, K.A., 1974. A random medium analysis of crust and upper mantle structure under NORSAR. Geophys. Res. Lett., 1: 327–328.

Dainty, A.M., 1981. A scattering model to explain seismic Q observations in the lithosphere between 1 and 30 Hz. Geophys. Res. Lett., 11: 1126–1128.

Dainty, A.M., 1984. High-frequency acoustic backscattering and seismic attenuation. J. Geo-

phys. Res., 89: 3172–3176.

Dainty, A.M., 1985. Coda Observed at NORSAR and NORESS. Final Rep. AFGL-TR-85-0199, Air Force Geophysics Lab., Hanscom AFB, MA, ADA166454.

Dainty, A.M., 1989. Studies of coda using array and three-component processing. PAGEOPH, in press.

Dainty, A.M. and Harris, D.B., 1989. Phase velocity estimation of diffusely scattered waves. Bull. Seis. Soc. Am., 79: 1231–1250.

Der, Z., Marshall, M.E., O'Donnell, A. and McElfresh, T.W., 1984. Spatial coherence structure and attenuation of the Lg phase, site effects, and interpretation of the Lg coda. Bull. Seis. Soc. Am., 74: 1125–1147.

Dysart, P.S. and Pulli, J.J., 1987. Spectral study of regional earthquakes and chemical explosions recorded at the NORESS array. In: Tech. Rep. for the Period 1 April—30 June 1987, Tech. Rep. C87-03, Center for Seismic Studies, Arlington VA, pp. 3-21—3-44.

Farjoodi, J., Sato, N. and Katayama, T., 1985. Engineering properties of ground motion obtained from dense seismograph array data (Part I: ground strain). Bull. Earthquak Resistant Structure Res. Center, #18: 9–30.

Flatté, S.M. and Wu, R.-S., 1988. Small-scale structure in the lithosphere and asthenosphere deduced from arrival time and amplitude fluctuations at NORSAR. J. Geophys. Res., 93: 6601–6614.

Flatté, S.M., Dashen, R., Munk, W.H., Watson, K.M. and Zachariasen, F., 1979. Sound

Transmission through a Fluctuating Ocean. Cambridge University Press, New York.

Frankel, A. and Clayton, R., 1986. Finite difference simulations of seismic scattering: implications for the propagation of short-period seismic waves in the crust and models of crustal heterogeneity. J. Geophys. Res., 91: 6465-6489.

Harichandran, R.S. and Vanmarcke, E.H., 1986. Stochastic variation of earthquake ground motion in space and time. J. Eng. Mech. ASCE, 112: 154-174.

Herrmann, R.B., 1980. Q estimates using the coda of local earthquakes. Bull. Seis. Soc. Am., 70: 447-468.

Ingate, S.F., Husebye, E.S. and Christoffersson, A., 1985. Regional arrays and processing schemes. Bull. Seis. Soc. Am., 75: 1155-1177.

Jenkins, G.M. and Watts, D.G., 1969. Spectral Analysis and its Applications. Holden-Day.

Kennett, B.L.N., 1986. Wavenumber and wavetype coupling in laterally heterogeneous media. Geophys. J. R. Astr. Soc. 87, 313-331.

Korhonen, H., Pirhonen, S., Ringdal, F., Mykkeltveit, S., Kværna, T., Larsen, P.W. and Paulsen, R., 1987. The FINESA array and preliminary results of data analysis. Inst. Seis., Univ. Helsinki, Rep. S-16.

Loh, C.-H., 1985. Analysis of the spatial variation of seismic waves and ground movements from SMART-1 array data. Earthquake Eng. Struc. Dyn., 13: 561-581.

Mandelbrot, B.B., 1977. Fractals. W.H. Freeman, San Francisco.

Mykkeltveit, S., Ringdal, F., Fyen, J. and Kværna, T., 1987. Initial results from analysis

21

of data recorded at the new regional array in Finnmark, Norway. In: L.B. Loughran
(Editor), Semiann. Tech. Sum., 1 April—30 Sept. 1987, NORSAR Sci. Rep. #1-87/88.

Tatarskii, V.I., 1961. Wave Propagation in a Turbulent Medium. McGraw-Hill, New York.

Toksöz, M.N., Dainty, A.M. and Charrette, E.E., 1989. Spatial variation of ground motion
due to lateral heterogeneity. Structural Safety, in press.

Vanmarcke, E.H., 1983. Random Fields: Analysis and Synthesis. M.I.T. Press, Cambridge.

Virieux, J., 1984. SH-Wave propagation in heterogeneous media: velocity-stress finite-difference
method. Geophysics, 49: 1933–1957.

Virieux, J., 1986. P-SV wave propagation in heterogeneous media: velocity-stress finite-difference method. Geophysics, 51: 889–901.

Wu, R.-S., 1982. Attenuation of short period seismic waves due to scattering. Geophys. Res.
Lett., 9: 9–12.

Wu, R.-S. and Aki, K., 1985. Elastic wave scattering by a random medium and the small
scale inhomogeneities in the lithosphere. J. Geophys. Res., 90: 10261–10273.

Table 1: Array locations.

Array	Latitude	Longitude	No. of Elements
ARCESS	69.535N	25.506E	25
FINESA	61.444N	26.079E	10
NORESS	60.735N	11.541E	25

Table 2: Events Analysed. Azimuth (from N) and Velocity are estimated from frequency-wavenumber analysis, not locations.

Date	OT (UTC)	Lat.	Long.	Location	Recorded	Dist. (km)	Az.	Velocity (km/s)
27 Feb. 1985	12:58:31	59.3N	6.5E	Blåsjø[a]	NORESS	324	243°	3.8
15 Nov. 1985	13:53:37	61.1N	29.9E	Leningrad[b]	FINESA	209	99°	3.6
6 Feb. 1986	12:22:04	59.3N	28.1E	Leningrad[c]	FINESA	264	151°	4.5
16 Dec. 1987	11:48:54	68.1N	33.2E	Kola[d]	ARCESS	350	116°	4.1

[a]Blåsjø Quarry location from Dysart and Pulli (1987). OT from S—P time.
[b]OT and location from Ahjos et al. (1986a)
[c]OT and location from Ahjos et al. (1986b)
[d]Quarry location from Mykkeltveit et al. (1987). OT from S—P time.

FIGURE CAPTIONS

Figure 1: Geophone array configurations at FINESA (top) and NORESS and ARCESS (bottom)

Figure 2: Vertical component seismograms recorded at FINESA 15 Nov. 1985 from a quarry blast at 209 km range.

Figure 3: The squared Fourier spectrum and the frequency-wavenumber analysis for the windowed portion of the data in Figure 2.

Figure 4: Coherency vs distance at 2 Hz (top), 4 Hz (middle) and 6 Hz (bottom) for the windowed data in Figure 2.

Figure 5: The phase lag vs distance at 2 Hz (top), 4 Hz (middle) and 6 Hz (bottom) for the windowed data in Figure 2.

Figure 6: Vertical component seismograms recorded at FINESA 6 Feb. 1986 (top), ARCESS 16 Dec. 1987 (middle) and NORESS 27 Feb. 1985 (bottom) center seismometers with analysis windows indicated.

Figure 7: Coherency vs distance at 2 Hz (top), 4 Hz (middle) and 6 Hz (bottom) for the NORESS windowed data in Figure 6.

Figure 8: Coherency vs distance normalized to the wavelength for events recorded at FINESA.

Figure 9: Coherency vs normalized distance for events recorded at ARCESS (top) and NORESS (bottom).

Figure 10: Randomized time series. Top trace is taken from analysis window of top trace of Figure 2. Succeeding traces are produce by iterative, random perturbations of Fourier phase of top trace. See text for discussion.

Figure 11: Fourier phase perturbations (radians) used to produce second trace from the top in Figure 10 from the top trace. Perturbations are added to the phase. See text for discussion.

Figure 12: Coherency vs distance for the randomized traces in Figure 10 at 4 Hz. The distance scale was constructed by considering each trace in Figure 10 to be part of a linear array of spacing 200 m.

Figure 13: (Top) Model used for synthetic computations. The source is explosive and seismograms are computed for an array 2 km long with a spacing of 125 m. Dimensions of the model are 6.5×25 km; the upper layer has a P velocity of 6 km/s, the lower 7 km/s and Poisson's ratio is 0.25. (Bottom) Vertical seismograms for a wavelet of dominant frequency 3 Hz, lagged at 4.5 km/s and with an analysis window indicated. Top number to right of each trace is the element number (01 is at 22 km, 17 at 24 km) and the bottom number is the maximum ampllitude.

Figure 14: Coherency vs distance at 3 Hz for the vertical component synthetic seismograms of Figure 13.

Figure 15: Coherency vs normalized distance for the 27 Feb. 1985 event recorded at NORESS and the synthetic seismograms of Figure 13. See text for discussion.
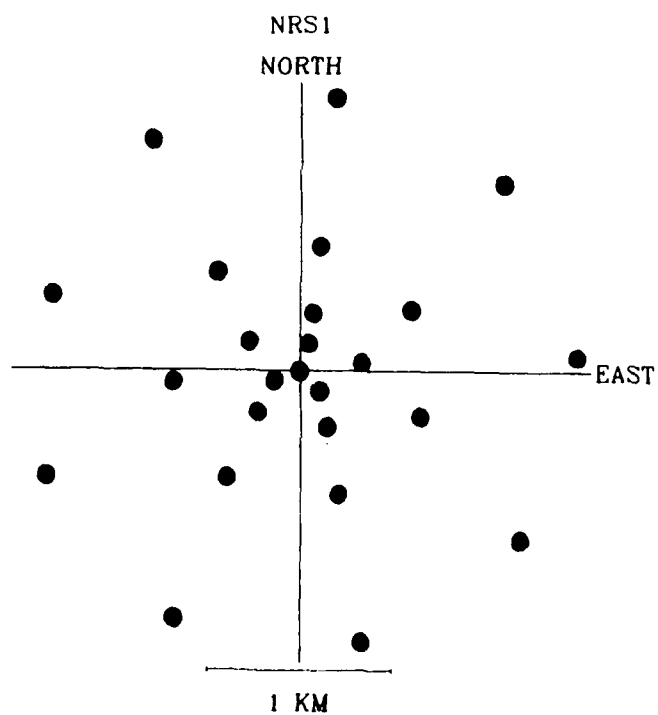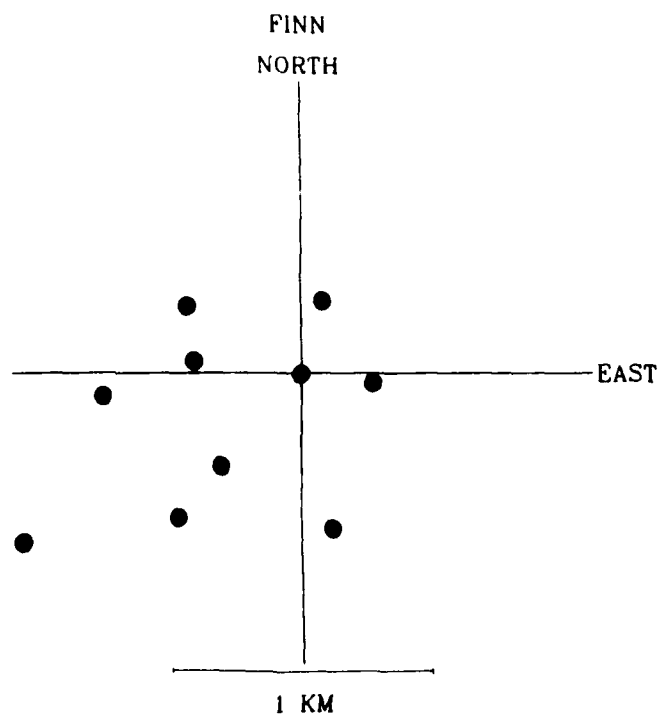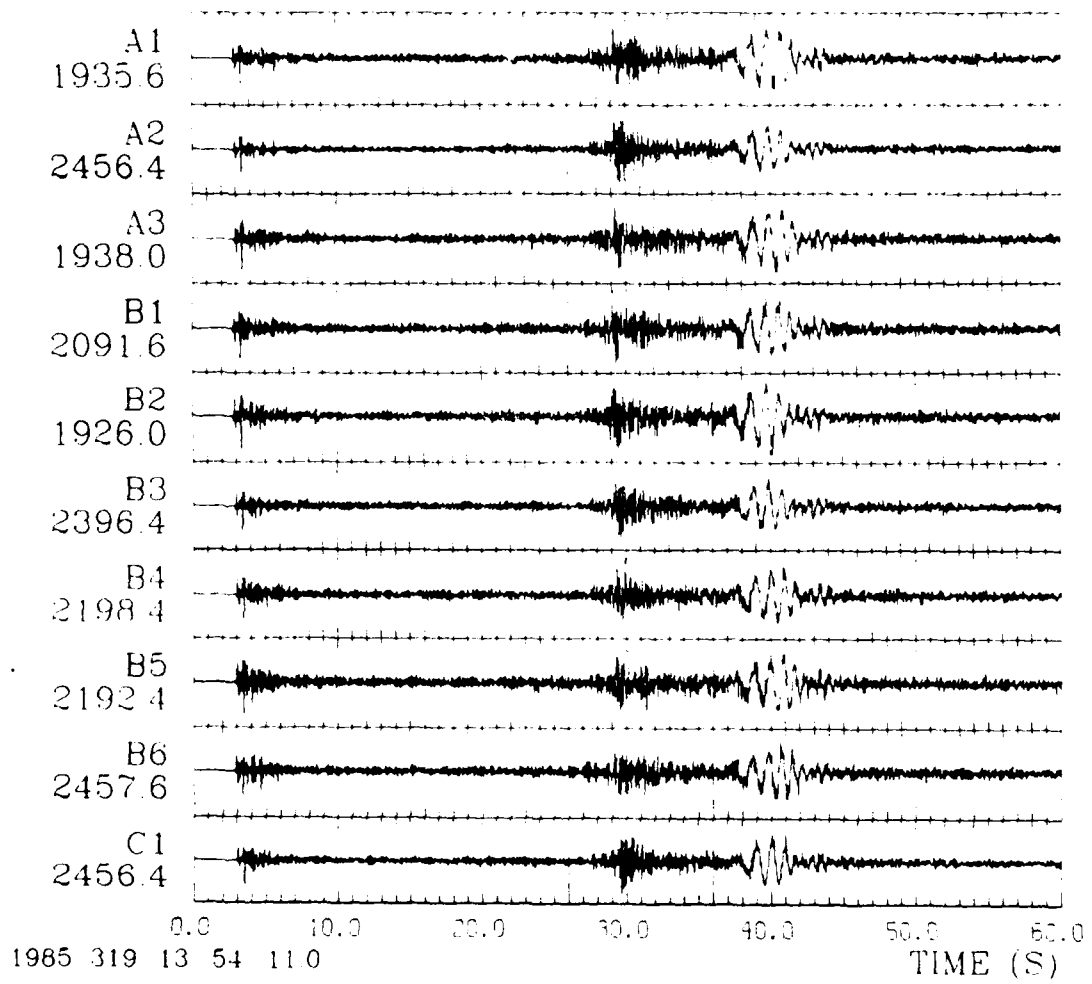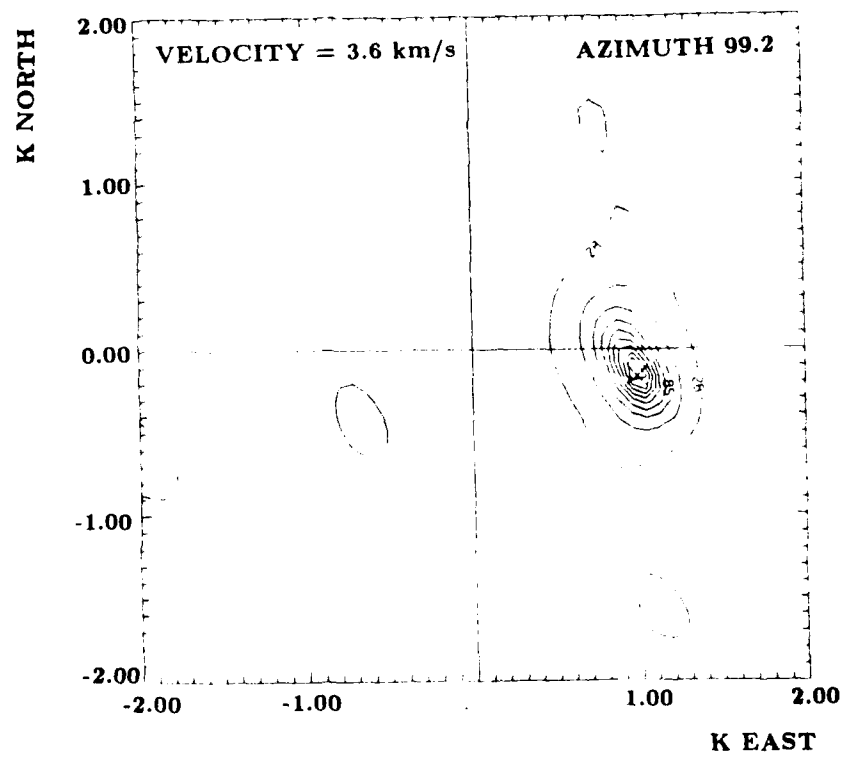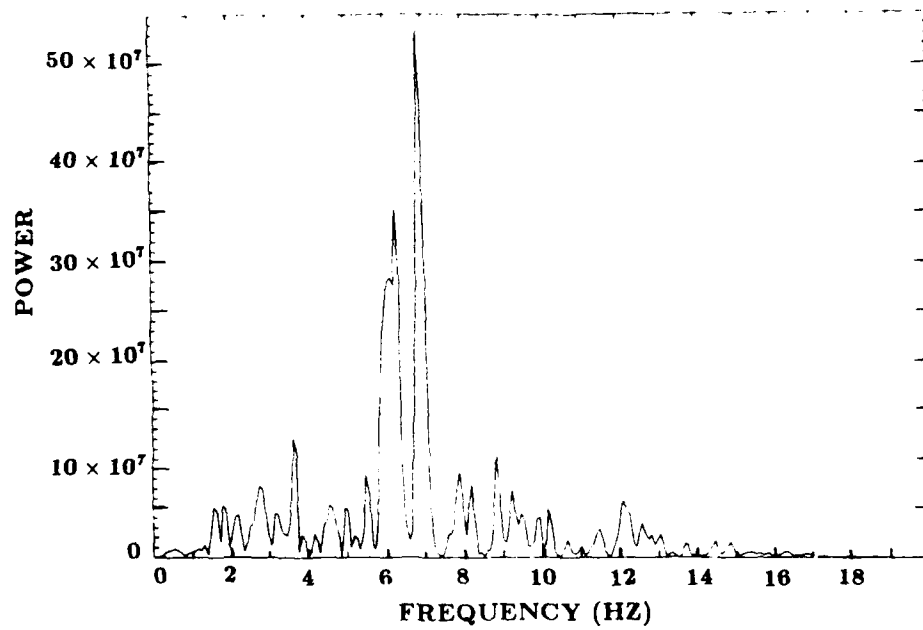
Figure 1.

26

F85319

Figure 2.

Figure 3.

Figure 4.

Figure 5.

30

F860337

A1
2456 4

1986 37 12 22 44 0   TIME (S)

E872250

A0
594210

1987 350 11 49 15 0   TIME (S)

N85058

A0
47059 2

1985 58 12 58 16 0   TIME (S)

Figure 6.

31

Figure 7.

32

F85319

Normalized Distance (Wavelengths)

F86037

Normalized Distance (Wavelengths)

Figure 8.

33

K87350

Normalized Distance (Wavelengths)

N85058

Normalized Distance (Wavelengths)
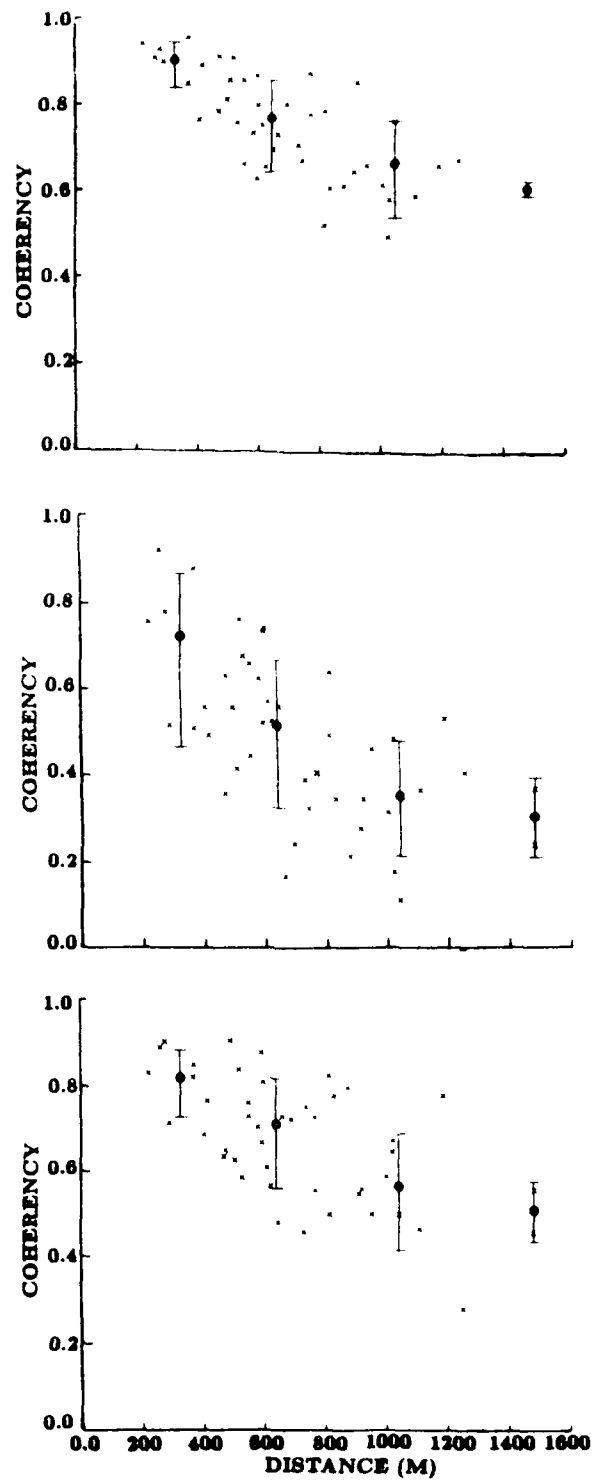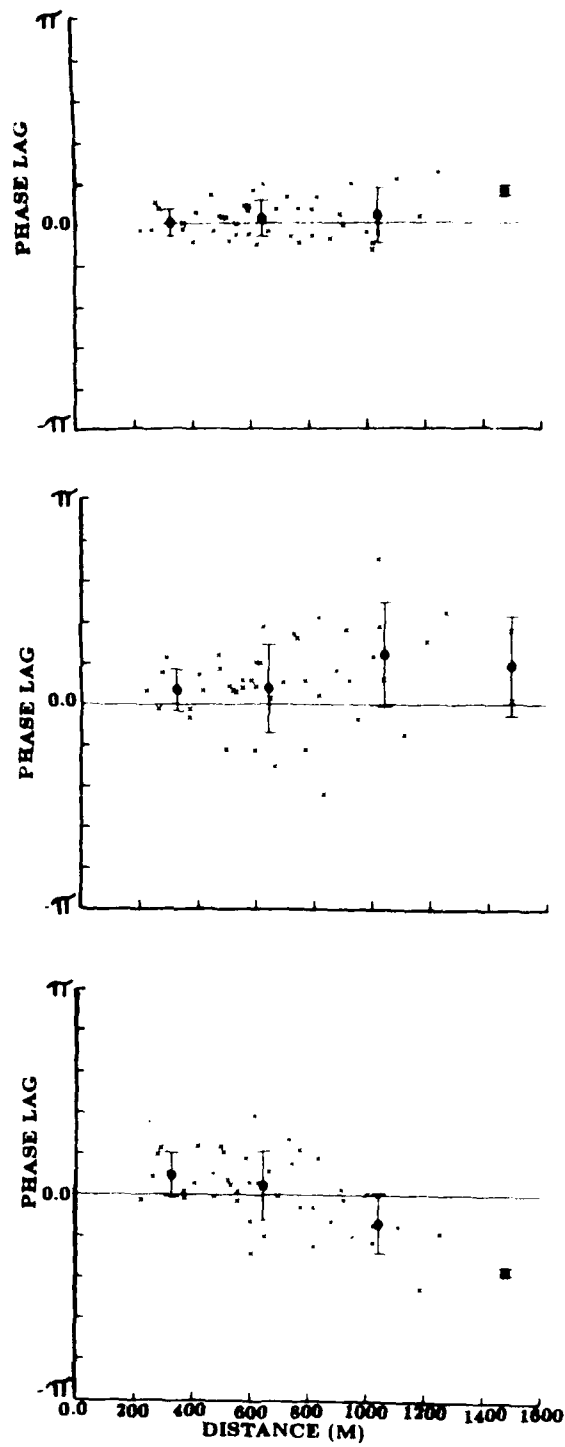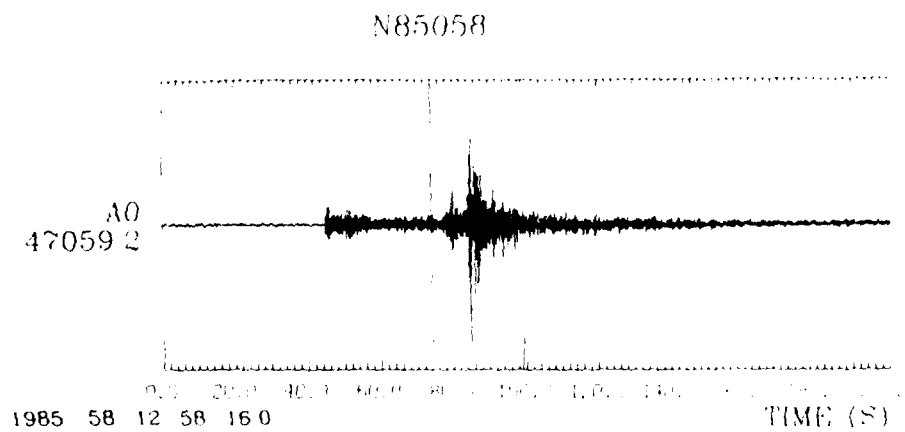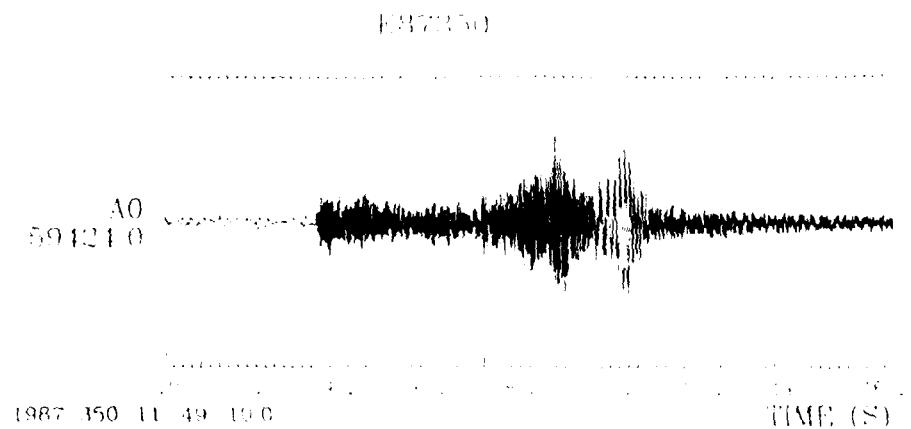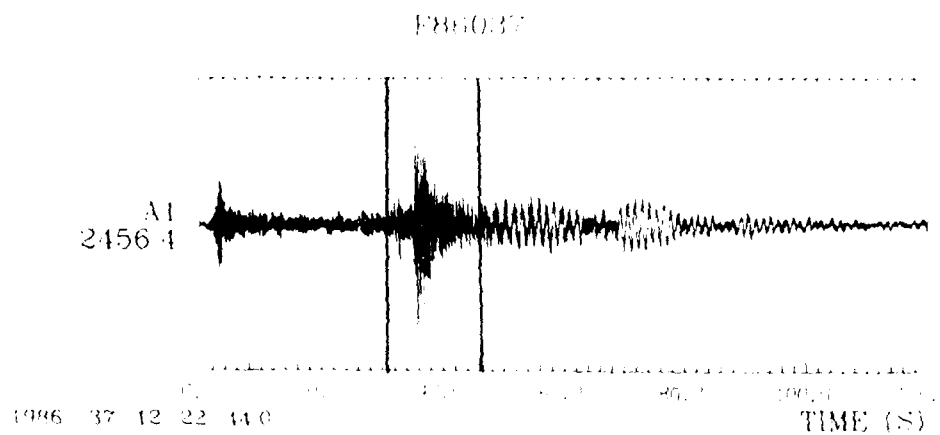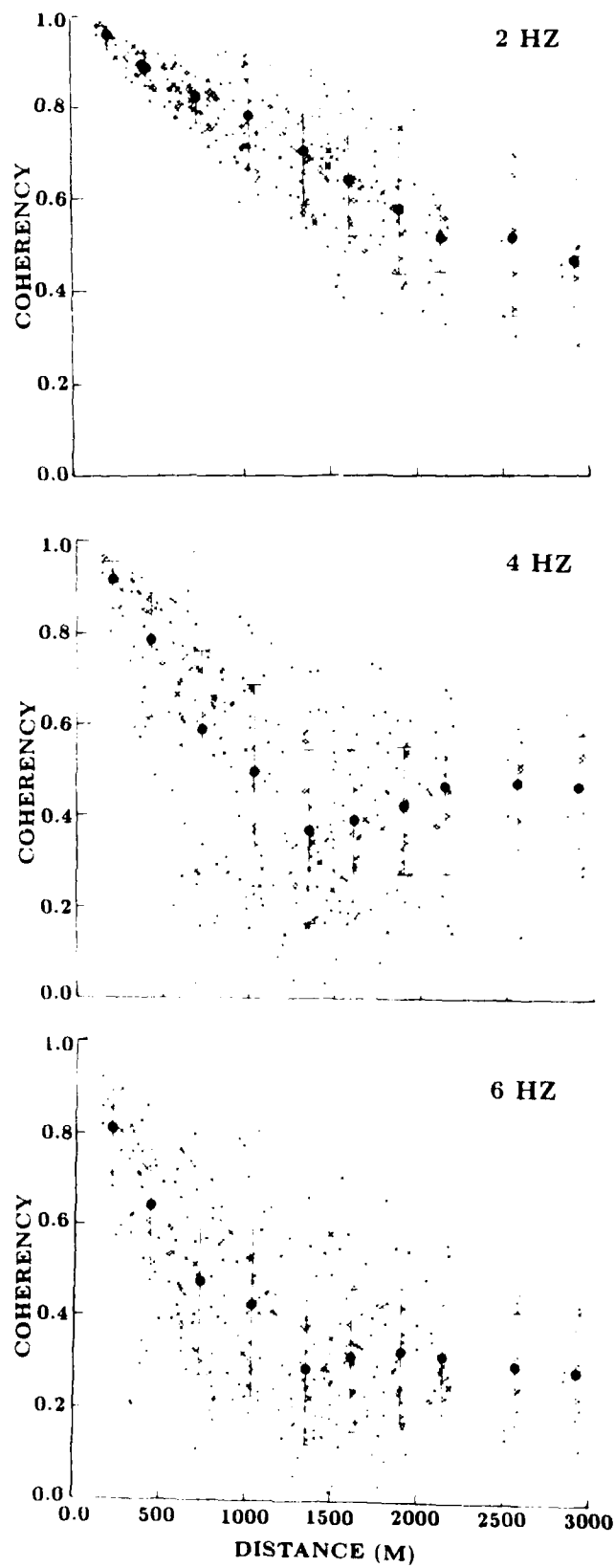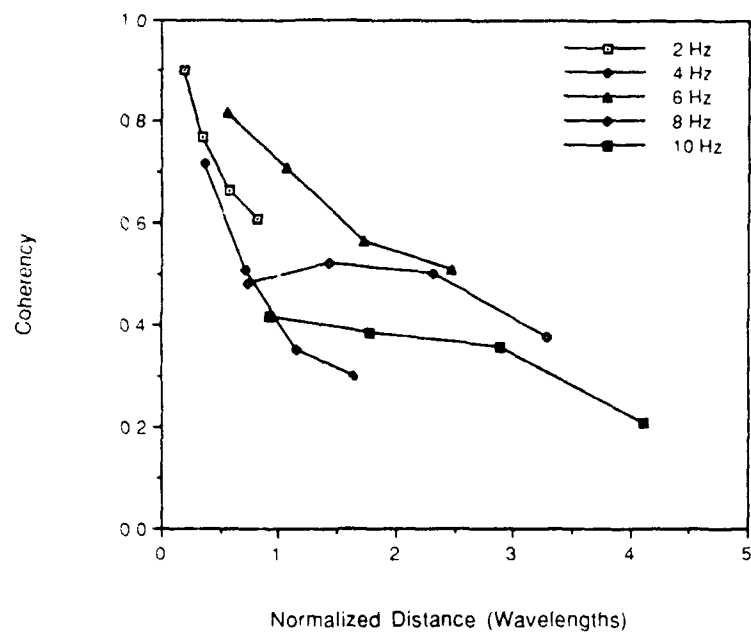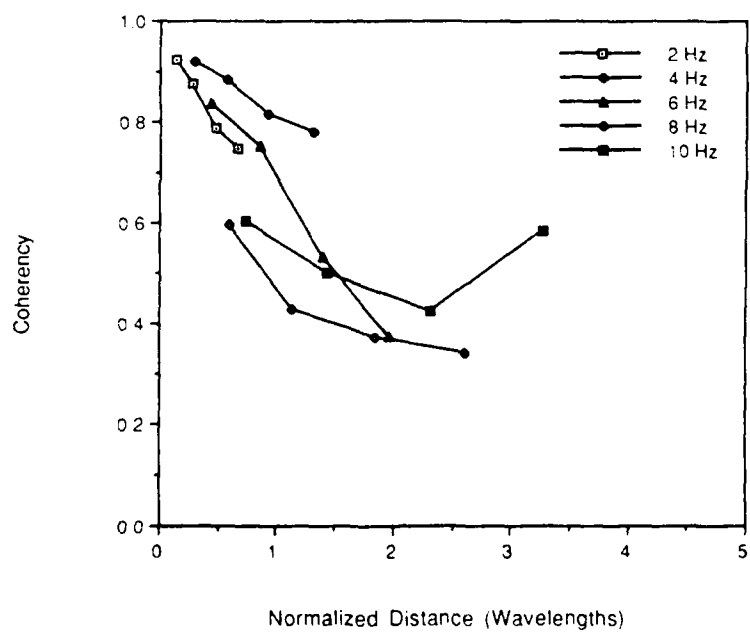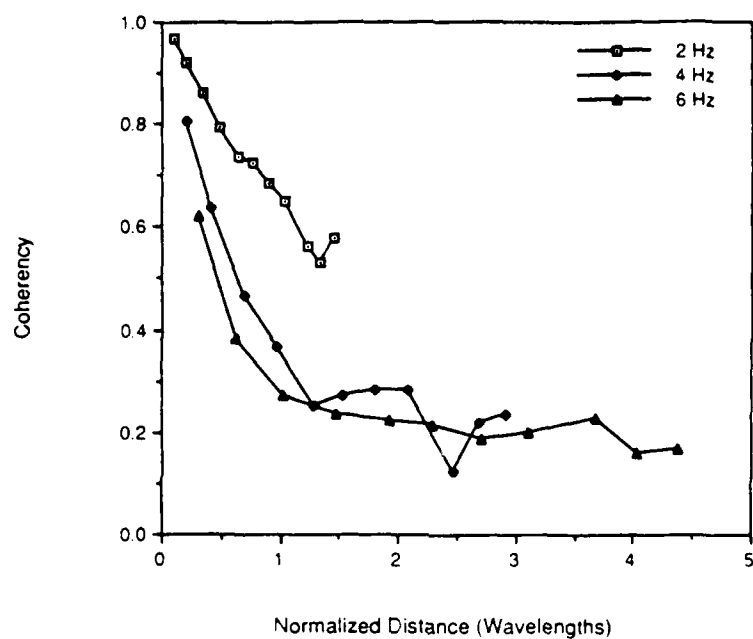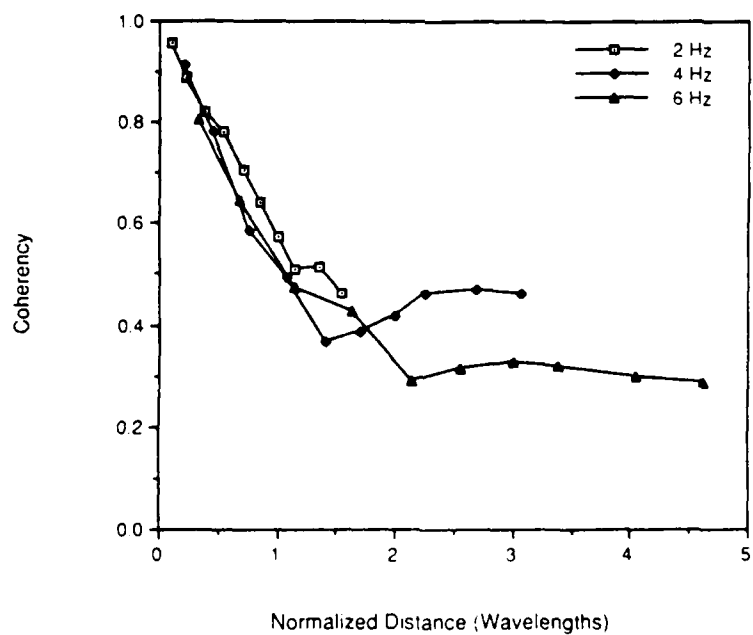
Figure 9.

TRAVEL TIME 0.04 SEC


```
01
1935 6

02
1771.3

03
1462.9

04
1399.0

05
1303.5

06
1294.4

07
1638.7

08
1539 2

09
1681.2

10
1394.4
```

```
0.0    1.1    2.1    3.2    4.3    5.3    6.4
```

1985 319 13 54 38 3   TIME (S)

Figure 10.

35
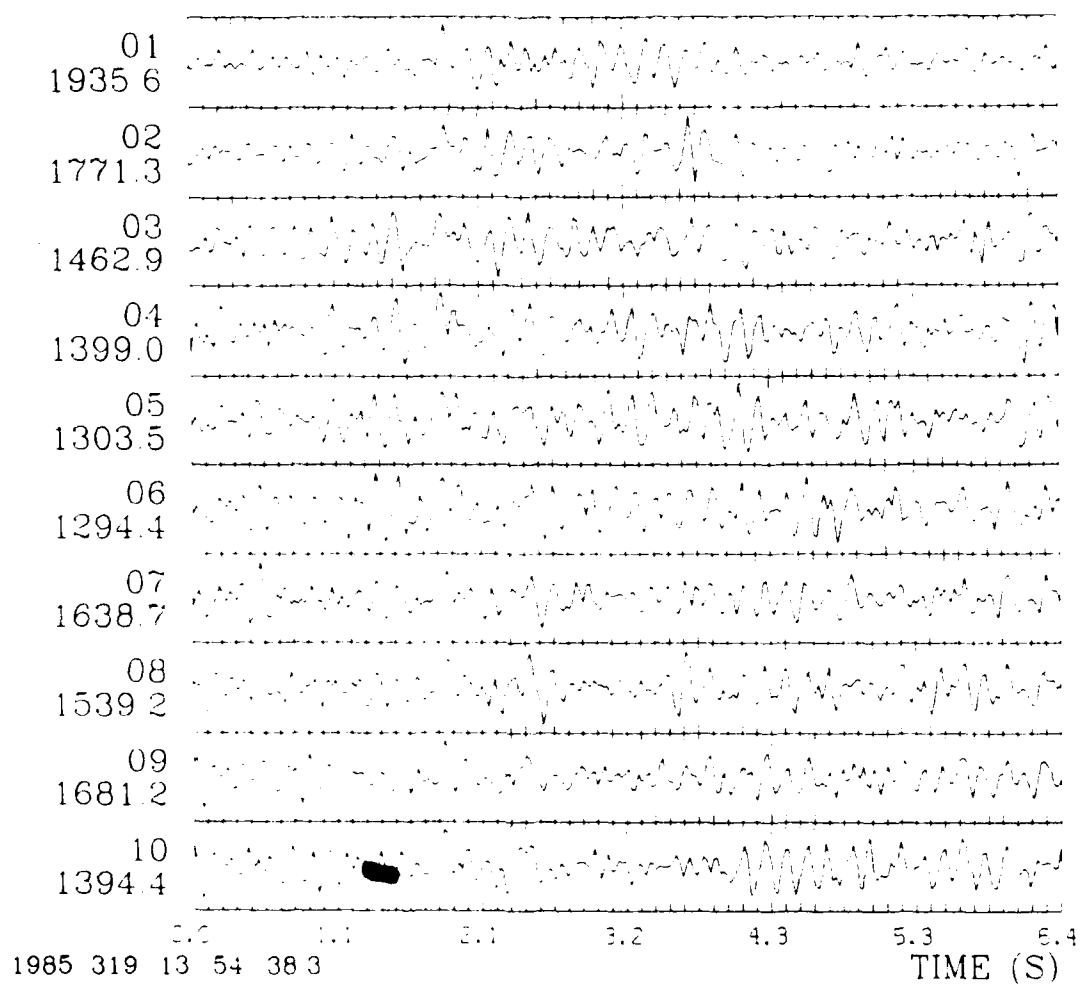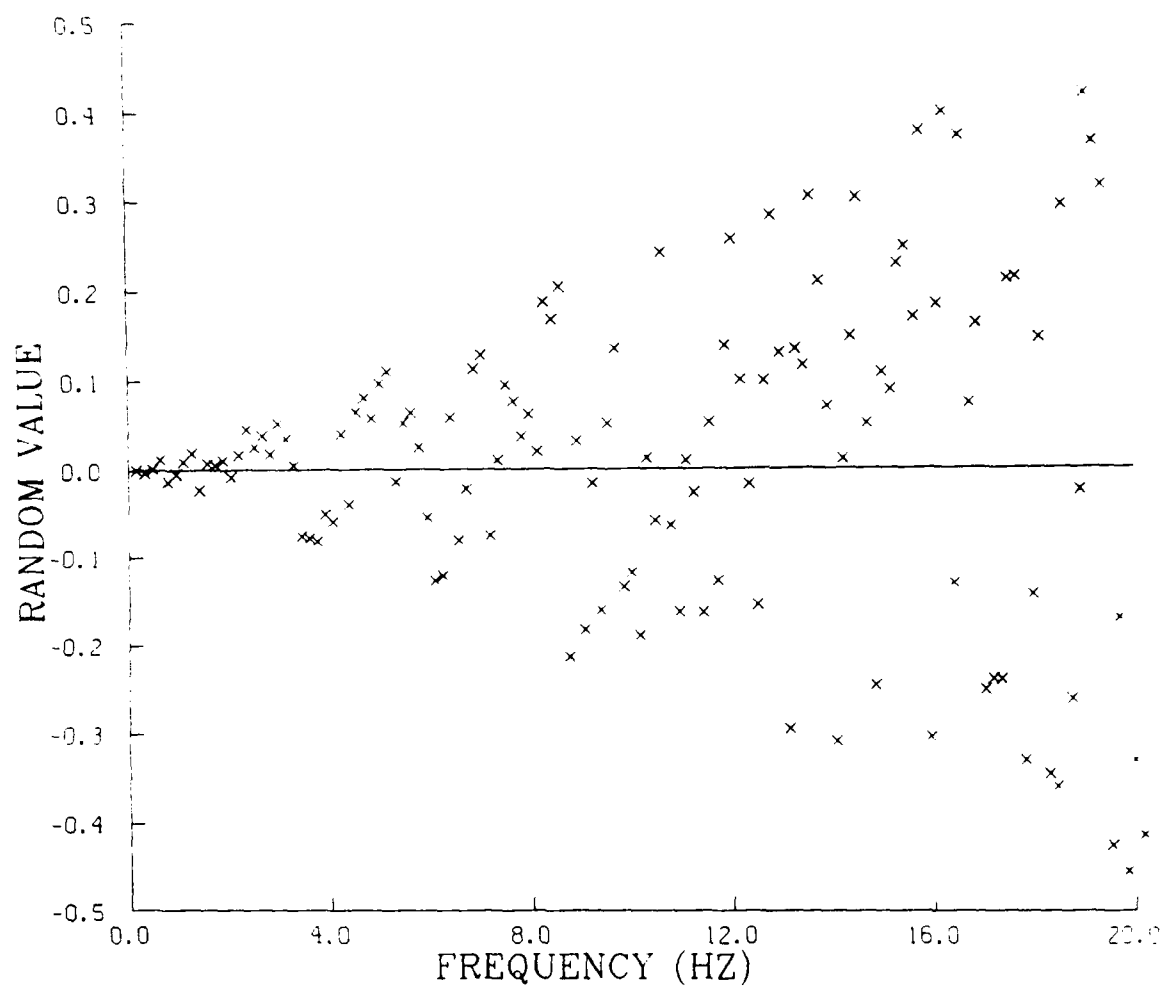
TRAVEL TIME 2

Figure 11.

TRAVEL TIME 0.04 SEC 4 HZ
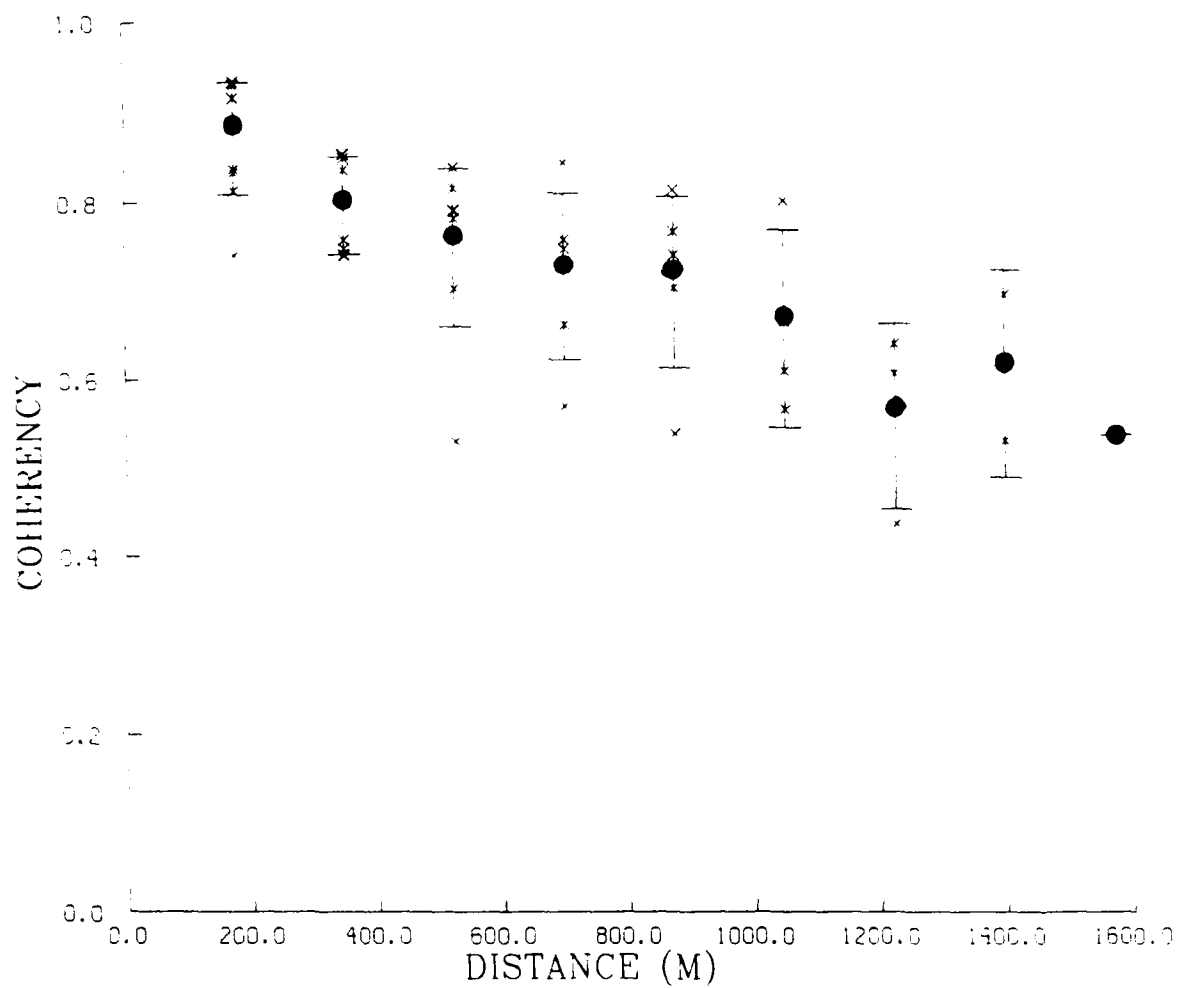
Figure 12.

Self Similar Model with 15% Perturbations

P wave velocity (km/s)

5   7

SYNTHETIC VERTICAL SHIFTED   SYNTHETIC VERTICAL SHIFTED

Figure 13.

38

SYNTHETIC VERTICAL
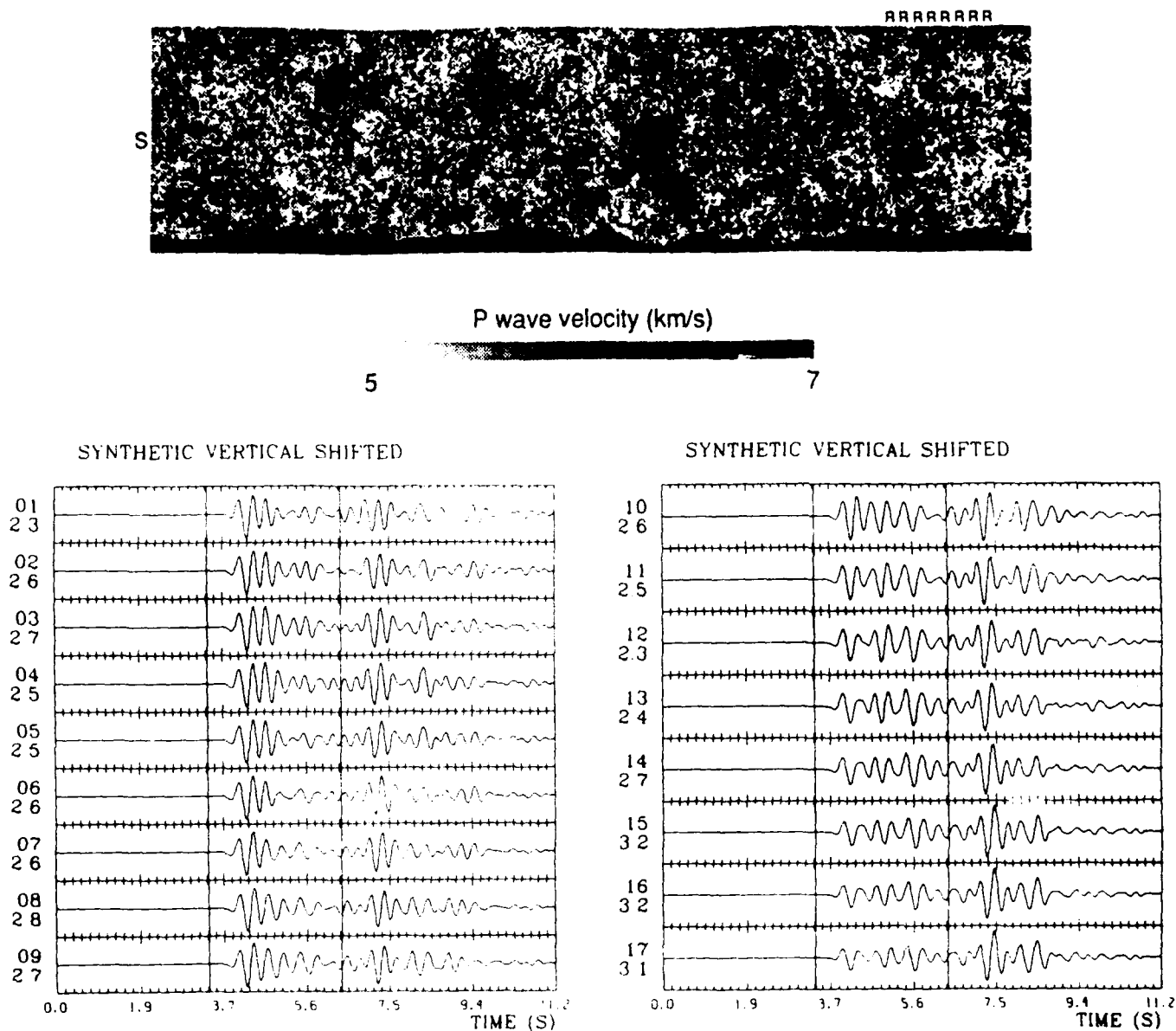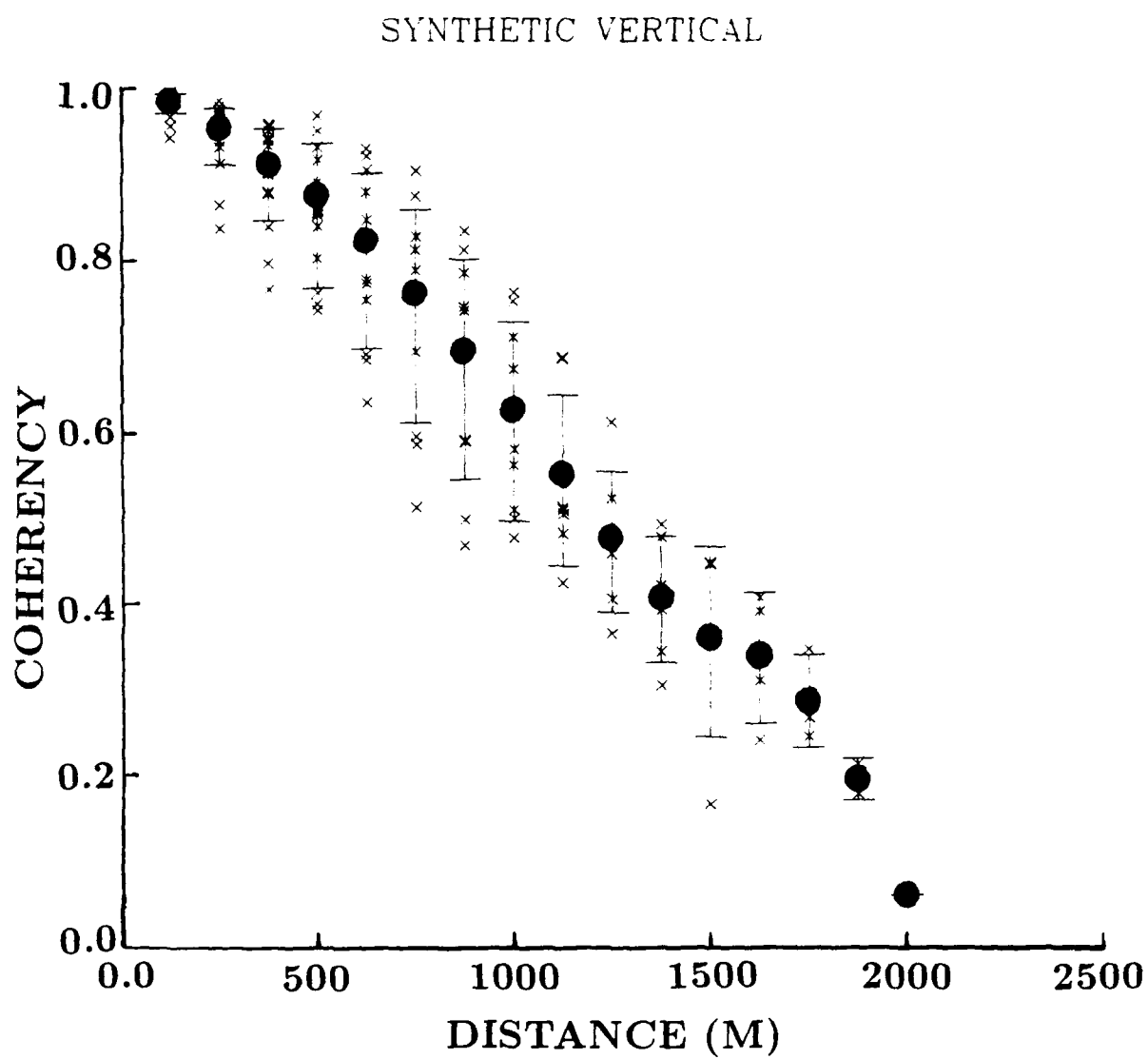
Figure 14.

N85058
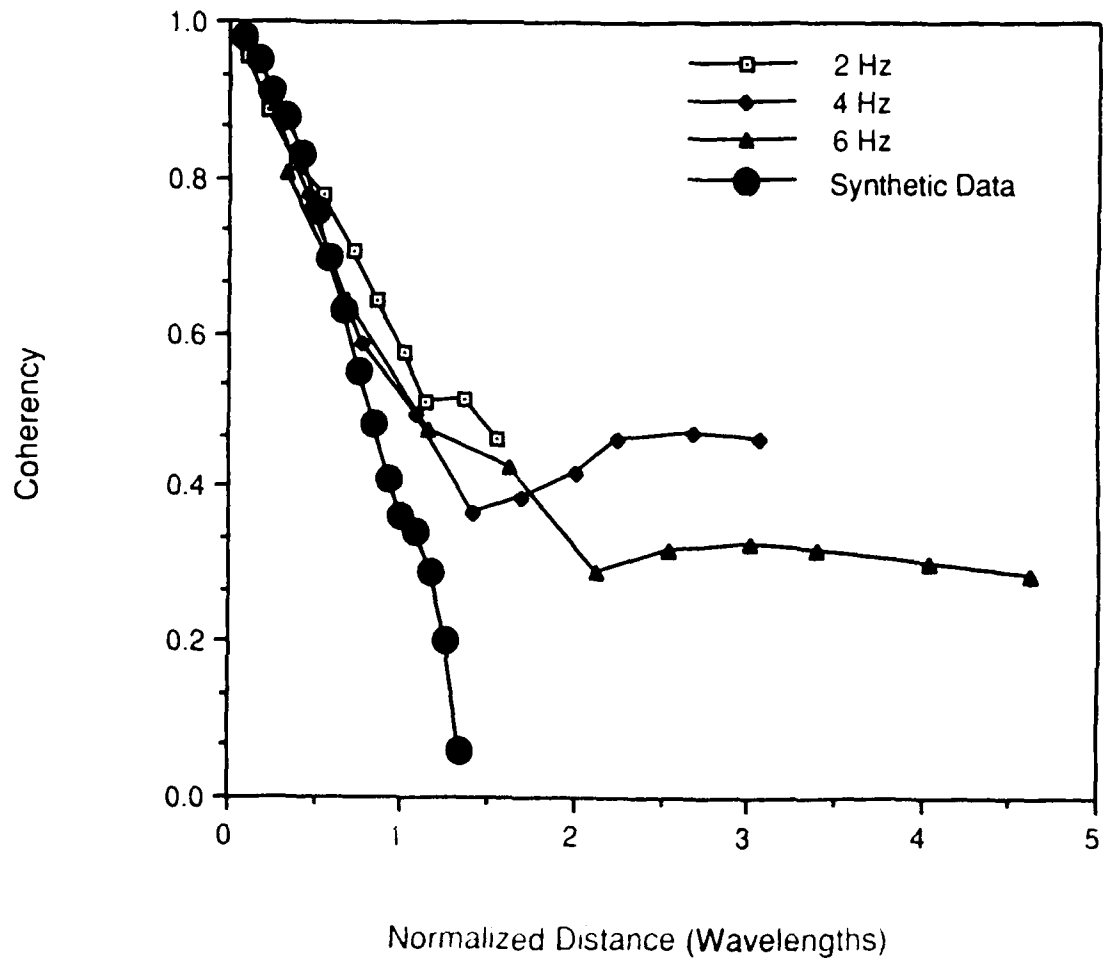
Figure 15.

SCATTERING OF ELASTIC WAVES BY

LOCALIZED ANISOTROPIC INCLUSIONS

by

Ari Ben-Menahem[1] and Richard L. Gibson, Jr.

Earth Resources Laboratory

Department of Earth, Atmospheric, and Planetary Sciences

Massachusetts Institute of Technology

Cambridge, MA 02139

[1]NRC Fellow. Earth Sciences Division, Air Force Geophysical Laboratory, Hanscom Air Force Base, MA 02731. On leave from the Weizmann Institute of Science, Rehovot, Israel 76100.

41

Abstract

The existence of Rayleigh-scattering of elastic plane-waves by anisotropic homogeneous inclusions is theoretically demonstrated. The case of transverse isotropy is studied in detail. It is shown that a scattered longitudinal wave creates radial-longitudinal (P), collatitudinal-shear (SV) and azimuthal shear waves (SH). Likewise, scattered SV and SH waves generate each, radial P waves, SV and SH shear waves. All scattered amplitudes are proportional to the square of the frequency and have radiation pattern signatures as those of equivalent dipoles, center of compression and double couples. It is shown that observations of spatial patterns of scattered amplitudes can yield through inversion, the elastic constants of the anisotropic inclusion. Our results can serve as a theoretical basis for the observed short-period SH and SV waves from underground explosions at teleseismic distances.

42

INTRODUCTION

Elastic wave scattering by elastic heterogeneities, using the equivalent source method and Born approximation has been successfully formulated and applied to acoustics and seismology (Gubernatis *et al.*, 1977; Haddon and Cleary, 1974; Wu and Aki, 1985). Recently, Ben-Menahem (1989a, 1989b) obtained the explicit analytic Green's tensor with the ensuing displacements fields due to unipolar and dipolar point sources in azimuthally-isotropic media. In the present paper, we combine the results of the above two disciplines to show that the method can be generalized to include scattering due to a combined elastic heterogeneity and anisotropy having slightly different elastic constants from the surrounding medium. In particular, we work out in detail the scattering due to a small azimuthally-isotropic inclusion. We show that scattered field is equivalent to those generated by point dipoles and double couples. The most important results of our study is that a few scattering experiments, through which plane P, SH and SV waves are sent to interact with the inclusion, lead to the determination of the elastic constants of the inclusion. We hope that this will become useful in exploration geophysics where azimuthal-isotropy is linked to the presence of shale (Winterstein, 1986). Also, it may explain the presence of SH and SV waves in the near and far fields of underground chemical and nuclear explosions (Kisslinger *et al.*, 1961; Gupta and Blandford, 1983).

43

1. EQUIVALENT SOURCES FOR FIRST-ORDER SCATTERERS

Consider an homogeneous anisotropic elastic solid of density ρ. The force-free Cauchy equation of motion for this solid is (e.g., Ben-Menahem and Singh, 1981),

$$div \ \overleftrightarrow{T} - \rho \frac{\partial^2 \vec{u}}{\partial t^2} = 0 \tag{1.1}$$

where $\overleftrightarrow{T}(\vec{u})$ is the stress tensor, and $\vec{u}(\vec{r}, t)$ are the spectral displacements.

We choose a Cartesian coordinate system $O(x, y, z)$ in which xy is the plane of isotropy. In matrix notation, the stress tensor for azimuthally isotropic media bears the explicit matrix form (Love, 1944)

$$T_{jk} = \begin{bmatrix} C_{11}\frac{\partial u_x}{\partial x} + C_{12}\frac{\partial u_y}{\partial y} + C_{13}\frac{\partial u_z}{\partial z} & C_{66}\left(\frac{\partial u_x}{\partial y} + \frac{\partial u_y}{\partial x}\right) & C_{44}\left(\frac{\partial u_x}{\partial x} + \frac{\partial u_z}{\partial z}\right) \\ \\ C_{66}\left(\frac{\partial u_x}{\partial y} + \frac{\partial u_y}{\partial x}\right) & C_{12}\frac{\partial u_x}{\partial x} + C_{11}\frac{\partial u_y}{\partial y} + C_{13}\frac{\partial u_z}{\partial z} & C_{44}\left(\frac{\partial u_z}{\partial y} + \frac{\partial u_y}{\partial z}\right) \\ \\ C_{44}\left(\frac{\partial u_x}{\partial x} + \frac{\partial u_z}{\partial z}\right) & C_{44}\left(\frac{\partial u_z}{\partial y} + \frac{\partial u_y}{\partial z}\right) & C_{13}\left(\frac{\partial u_x}{\partial x} + \frac{\partial u_y}{\partial y}\right) + C_{33}\frac{\partial u_z}{\partial z} \end{bmatrix} \tag{1.2}$$

Here, (u_x, u_y, u_z) are the Cartesian displacement components and $\{\rho, C_{11}, C_{13}, C_{33}, C_{44}, C_{66}, C_{12} = C_{11} - 2C_{66}\}$ are six independent structural parameters of the medium. The matrix relation in Eq. (1.2) can be put in the convenient tensor form

$$\overleftrightarrow{T} = [C_{13} \ \overleftrightarrow{I} \ div \ \vec{u} + C_{44}(\vec{\nabla}\vec{u} + \vec{u}\vec{\nabla})] + \overleftrightarrow{T}_{anisotropic} , \tag{1.3}$$

44

$$\overset{\leftrightarrow}{T}_{anisotropic} = (C_{11} - C_{13} - 2C_{44}) \, (\overset{\leftrightarrow}{I} - \vec{e}_z \vec{e}_z) \left(\frac{\partial u_x}{\partial x} + \frac{\partial u_y}{\partial y} \right) + \tag{1.4}$$

$$+ (C_{33} - C_{13} - 2C_{44}) \, \frac{\partial u_z}{\partial z} \, \vec{e}_z \vec{e}_z$$

$$+ (C_{44} - C_{66}) \left[2\frac{\partial u_x}{\partial x} \vec{e}_y \vec{e}_y + 2\frac{\partial u_y}{\partial y} \vec{e}_x \vec{e}_x - \left(\frac{\partial u_x}{\partial y} + \frac{\partial u_y}{\partial x} \right) (\vec{e}_x \vec{e}_y + \vec{e}_y \vec{e}_x) \right] \, .$$

Consider an anisotropic obstacle of structural parameters $\{ \rho; \ C_{11}; \ C_{13}; \ C_{33}; \ C_{44}; \ C_{66} \}$ embedded in an infinite isotropic elastic space with parameters

$$C_{11}^{(0)} = C_{33}^{(0)} = \lambda + 2\mu \; ; \quad C_{44}^{(0)} = C_{66}^{(0)} = \mu \; ; \quad (C_{13})^0 = \lambda \, .$$

Let

$$C_{ij} = C_{ij}^{(0)} + \delta C_{ij} \tag{1.5}$$

where δC_{ij} are small perturbations such that $C_{ij} = C_{ij}^{(0)}$ in the isotropic limit. We assume that the obstacle is small compared with the wavelength of the impinging radiation. We put Eqs. (1.3) and (1.4) into Eq. (1.1) with C_{ij} given by Eq. (1.5), and assume a *perturbation solution* of Eq. (1.1) in the form $\vec{u} = \vec{u}^{(0)} + \vec{u}^1$, where $\vec{u}^{(0)}$ is a *primary field* and $\vec{u}^{(1)}$ is a scattered field. The equation of motion then splits into two simultaneous wave equations,

$$div \, \{ C_{13}^{(0)} I \, div \, \vec{u}^{(0)} + C_{44}^{(0)} (\vec{\nabla} \vec{u}^{(0)} + \vec{u}^{(0)} \vec{\nabla}) \} - \rho \frac{\partial^2 \vec{u}^{(0)}}{\partial t^2} = 0 \tag{1.6}$$

$$div \, \{ C_{13}^{(0)} I \, div \, \vec{u}^{(1)} + C_{44}^{(0)} (\vec{\nabla} \vec{u}^{(1)} + \vec{u}^{(1)} \vec{\nabla}) \} - \rho \frac{\partial^2 \vec{u}^{(1)}}{\partial z^2} = -div \, \overset{\leftrightarrow}{M} \tag{1.7}$$

where

$$\overset{\leftrightarrow}{M} = [\delta C_{11} - \delta C_{13} - 2\delta C_{44}] \left[\left(\frac{\partial u_x^{(0)}}{\partial x} + \frac{\partial u_y^{(0)}}{\partial y} \right) + (\delta C_{13}) div \, \vec{u}^{(0)} \right] \overset{\leftrightarrow}{I}$$

$$
+ \ [\delta C_{33} - \delta C_{13} - 2\delta C_{44}] \frac{\partial u_z^{(0)}}{\partial z} - [\delta C_{11} - \delta C_{13} - \delta C_{44}] \left(\frac{\partial u_x^{(0)}}{\partial x} + \frac{\partial u_y^{(0)}}{\partial y} \right) \vec{e}_z \vec{e}_z
$$

$$
+ \ [\delta C_{44} - \delta C_{66}] \left[2\frac{\partial u_x^{(0)}}{\partial x} \vec{e}_y \vec{e}_y + 2\frac{\partial u_y^{(0)}}{\partial y} \vec{e}_x \vec{e}_x - \left(\frac{\partial u_x^{(0)}}{\partial y} + \frac{\partial u_y^{(0)}}{\partial x} \right) \vec{e}_x \vec{e}_y + \vec{e}_y \vec{e}_x \right] \ +
$$

$$
+ \ \delta C_{44}[\vec{\nabla} \vec{u}^{(0)} + \vec{u}^{(0)} \vec{\nabla}] \ . \tag{1.8}
$$

The right-hand side of Eq. (1.7) indicates the presence of a dipolar point source with moment density $\vec{M}$ (Ben-Menahem and Singh, 1981, pp. 167–169; Tarantola *et al.*, 1988). Through this representation, $\vec{M}$ is identified as the equivalent source of the scattered field. Indeed, introducing the explicit expression for $[\vec{\nabla} \vec{u}^{(0)} + \vec{u}^{(0)} \vec{\nabla}]$, we may decompose $\vec{M}$ in Eq. (1.8) into five partial tensors, each of which represents a different force system:

I. Explosion

$$
\vec{M}_1 = (\delta C_{13}) \begin{bmatrix} div \ \vec{u}^{(0)} & 0 & 0 \\ \\ 0 & div \ \vec{u}^{(0)} & 0 \\ \\ 0 & 0 & div \ \vec{u}^{(0)} \end{bmatrix} \tag{1.9}
$$

46

II. Dipole along the symmetry axis (z)

$$\vec{\vec{M}}_2 = (\delta C_{33} - \delta C_{13}) \begin{bmatrix} 0 & 0 & 0 \\ 0 & 0 & 0 \\ 0 & 0 & \partial_z u_z^{(0)} \end{bmatrix} \tag{1.10}$$

III. Dipoles in the isotropy plane (xy)

$$\vec{\vec{M}}_3 = (\delta C_{11} - \delta C_{13}) \begin{bmatrix} \partial_x u_x^{(0)} + \partial_y u_y^{(0)} & 0 & 0 \\ 0 & \partial_x u_x^{(0)} + \partial_y u_y^{(0)} & 0 \\ 0 & 0 & 0 \end{bmatrix} \tag{1.11}$$

$$- 2(\delta C_{66}) \begin{bmatrix} \partial_y u_y^{(0)} & 0 & 0 \\ 0 & \partial_x u_x^{(0)} & 0 \\ 0 & 0 & 0 \end{bmatrix}$$

47

IV. Two double-couples on perpendicular saggital planes (xz, yz)

$$\vec{M}_4 = (\delta C'_{44}) \begin{bmatrix} 0 & 0 & \partial_x u_z^{(0)} + \partial_z u_x^{(0)} \\ 0 & 0 & \partial_y u_z^{(0)} + \partial_z u_y^{(0)} \\ \partial_x u_z^{(0)} + \partial_z u_x^{(0)} & \partial_y u_z^{(0)} + \partial_z u_y^{(0)} & 0 \end{bmatrix} \qquad (1.12)$$

V. Double-couple in the isotropy plane (xy)

$$\vec{M}_5 = (\delta C'_{66}) \begin{bmatrix} 0 & \partial_x u_y^{(0)} + \partial_y u_x^{(0)} & 0 \\ \partial_x u_y^{(0)} + \partial_y u_x^{(0)} & 0 & 0 \\ 0 & 0 & 0 \end{bmatrix} \qquad (1.13)$$

In the isotropic limit

$$\delta C_{13} = \delta\lambda \quad ; \quad \delta C_{33} - \delta C_{13} = \delta C_{11} - \delta C_{13} = 2\delta\mu \quad ; \quad \delta C_{44} = \delta C_{66} = \delta\mu , \qquad (1.14)$$

and we fall back on the known case of scattering due to a localized inhomogeneity (Wu and Aki, 1985). To this end, we can subdivide $\vec{M}$ in an alternative form, through which this

limit is immediately apparent. Using superscripts, we have:

$$
\overset{\leftrightarrow}{M}{}^{1} = \delta C_{13}
\begin{bmatrix}
\partial_x u_x^{(0)} + \partial_y u_y^{(0)} + \partial_z u_z^{(0)} & 0 & 0 \\[2em]
0 & \partial_x u_x^{(0)} + \partial_y u_y^{(0)} + \partial_z u_z^{(0)} & 0 \\[2em]
0 & 0 & \partial_x u_x^{(0)} + \partial_y u_y^{(0)} + \partial_z u_z^{(0)}
\end{bmatrix}
$$

$$(1.15)$$

$$
\overset{\leftrightarrow}{M}{}^{2} = \delta C_{44}
\begin{bmatrix}
\partial_x u_x^{(0)} & \partial_x u_y^{(0)} + \partial_y u_x^{(0)} & \partial_x u_z^{(0)} + \partial_z u_x^{(0)} \\[1.5em]
\partial_x u_y^{(0)} + \partial_y u_x^{(0)} & 2\partial_y u_y^{(0)} & \partial_y u_z^{(0)} + \partial_z u_y^{(0)} \\[1.5em]
\partial_x \partial u_z^{(0)} + \partial_z u_x^{(0)} & \partial_y u_z^{(0)} + \partial u_z u_y^{(0)} & 2\partial_z u_z^{(0)}
\end{bmatrix}
$$

$$(1.16)$$

$$
\overset{\leftrightarrow}{M}{}^{3} = (\delta C_{11} - \delta C_{13} - 2\delta C_{44})
\begin{bmatrix}
\partial_x u_x^{(0)} + \partial_y u_y^{(0)} & 0 & 0 \\[1.5em]
0 & \partial_x u_x^{(0)} + \partial_y u_y^{(0)} & 0 \\[1.5em]
0 & 0 & 0
\end{bmatrix}
$$

$$(1.17)$$

49

$$\overset{\leftrightarrow}{M}{}^{4} = (\delta C_{33} - \delta C_{13} - 2\delta C_{44}) \begin{bmatrix} 0 & 0 & 0 \\ \\ 0 & 0 & 0 \\ \\ 0 & 0 & \partial_z u_z^{(0)} \end{bmatrix} \qquad (1.18)$$

$$\overset{\leftrightarrow}{M}{}^{5} = (\delta C_{44} - \delta C_{66}) \begin{bmatrix} 2\partial_y u_y^{(0)} & -(\partial_x u_y^{(0)} + \partial_y u_x^{(0)}) & 0 \\ \\ -(\partial_x u_y^{(0)} + \partial_y u_x^{(0)}) & 2\partial_x u_x^{(0)} & 0 \\ \\ 0 & 0 & 0 \end{bmatrix} \qquad (1.19)$$

In the isotropic limit $\overset{\leftrightarrow}{M}{}^{3}$, $\overset{\leftrightarrow}{M}{}^{4}$, $\overset{\leftrightarrow}{M}{}^{5}$ vanish and $\overset{\leftrightarrow}{M}{}^{1}$, $\overset{\leftrightarrow}{M}{}^{2}$ survive to yield the scattering field due to a localized inhomogeneity.

2. THE SCATTERED FIELDS

For any given $\vec{u}^{(0)}$, the scattered field $\vec{u}^{(1)}$ solves Eq. (1.7) and is given approximately by Ben-Menahem and Singh (1981)

$$\vec{u}^{(1)} = -[\overleftrightarrow{M} : \vec{\nabla} \overleftrightarrow{G}^{(iso)}](\delta v) \tag{2.1}$$

where $\overleftrightarrow{G}^{(iso)}$ is the Green's tensor of the isotropic-homogeneous background matrix of the inclusion

$$\overleftrightarrow{G}^{(iso)} = \frac{1}{4\pi\mu} \left[\overleftrightarrow{I} \frac{e^{-ik_\beta R}}{R} + \vec{\nabla}\vec{\nabla} \frac{e^{-ik_\beta R} - e^{-ik_\alpha R}}{Rk_\beta^2} \right] \tag{2.2}$$

with

$$\mu = C_{44}^{(0)} \;\; ; \quad \lambda = C_{13}^{(0)} \;\; ; \quad k_\alpha^2 = \frac{\rho\omega^2}{\lambda + 2\mu} \;\; ; \quad k_\beta^2 = \frac{\rho\omega^2}{\mu}$$

and (δv) is the 'volume' of the obstacle.

Since $\vec{\nabla}\vec{\nabla} f(R) = (\vec{e}_\theta\vec{e}_\theta + \vec{e}_\phi\vec{e}_\phi)\frac{1}{R}\frac{\partial}{\partial R} + \vec{e}_R\vec{e}_R\frac{\partial^2}{\partial R^2}$, in spherical coordinates (R, θ, ϕ), we shall have in the 'far-field'

$$4\pi\mu \overleftrightarrow{G}^{(iso)} = \frac{\beta^2}{\alpha^2} \frac{e^{-ik_\alpha R}}{R}\vec{e}_R\vec{e}_R + \frac{e^{-ik_\beta R}}{R}(\vec{e}_\theta\vec{e}_\theta + \vec{e}_\phi\vec{e}_\phi) + 0\left[\frac{1}{k_\beta^2 R^2}\right] . \tag{2.3}$$

Substituting from Eq. (1.9)–(1.13) into Eq. (2.1), we obtain the five partial scattered fields,

$$\vec{u}_1^{(1)} = (\delta C_{13})(div\ \vec{u}^{(0)})div\ \overleftrightarrow{G} \tag{2.4}$$

$$\vec{u}_2^{(1)} = (\delta C_{33} - \delta C_{13}) \left(\frac{\partial u_z^{(0)}}{\partial z}\right) \frac{\partial}{\partial z}(\overleftrightarrow{G} \cdot \vec{e}_z) \tag{2.5}$$

51

$$\vec{u}_3^{(1)} = (\delta C_{11} - \delta C_{13}) \left(\frac{\partial u_x^{(0)}}{\partial x} + \frac{\partial u_y^{(0)}}{\partial y} \right) \left\{ \frac{\partial}{\partial x}(\vec{G} \cdot \vec{e}_x) + \frac{\partial}{\partial y}(\vec{G} \cdot \vec{e}_y) \right\}$$

$$- 2(\delta C_{66}) \left\{ \frac{\partial u_y^{(0)}}{\partial y} \frac{\partial}{\partial x}(\vec{G} \cdot \vec{e}_x) + \frac{\partial u_x^{(0)}}{\partial x} \frac{\partial}{\partial y}(\vec{G} \cdot \vec{e}_y) \right\} \tag{2.6}$$

$$\vec{u}_4^{(1)} = (\delta C_{44}) \left[\left(\frac{\partial u_z^{(0)}}{\partial x} + \frac{\partial u_x^{(0)}}{\partial z} \right) \left\{ \frac{\partial}{\partial x}(\vec{G} \cdot \vec{e}_z) + \frac{\partial}{\partial z}(\vec{G} \cdot \vec{e}_x) \right\} \right.$$

$$\left. + \left(\frac{\partial u_z^{(0)}}{\partial y} + \frac{\partial u_y^{(0)}}{\partial z} \right) \left\{ \frac{\partial}{\partial y}(\vec{G} \cdot \vec{e}_z) + \frac{\partial}{\partial z}(\vec{G} \cdot \vec{e}_y) \right\} \right] \tag{2.7}$$

$$\vec{u}_5^{(1)} = (\delta C_{66}) \left(\frac{\partial u_y^{(0)}}{\partial x} + \frac{\partial u_x^{(0)}}{\partial y} \right) \left\{ \frac{\partial}{\partial x}(\vec{G} \cdot \vec{e}_y) + \frac{\partial}{\partial y}(\vec{G} \cdot \vec{e}_x) \right\} \tag{2.8}$$

$$\overleftrightarrow{G} = \overleftrightarrow{G}^{(iso)}$$

(a) Incident P-wave $(\alpha = \sqrt{(\lambda + 2\mu)/\rho})$

Let

$$\vec{u}^{(0)} = U_0^{(p)} \vec{p} e^{i\omega\left[t - \frac{1}{\alpha}(y \sin\theta_0 + z \cos\theta_0)\right]} \equiv u_0^p \vec{p} , \tag{2.9}$$

where $\vec{p}$ is the wave's normal and θ_0 is the angle that $\vec{p}$ makes with the symmetry axis z (Figure 1). Due to the azimuthal symmetry of the scattering obstacle, we can choose, without loss of generality

$$\vec{p} = \vec{e}_y \sin\theta_0 + \vec{e}_z \cos\theta_0 \quad , \quad k_\alpha = \frac{\omega}{\alpha} . \tag{2.10}$$

Suppressing the factor $e^{i\omega t}$, the partial wave derivatives, needed for Eqs. (2.4)–(2.8), are:

$$u_x^{(0)} = 0 \; ; \; \frac{\partial u_x^{(0)}}{\partial x} = \frac{\partial u_x^{(0)}}{\partial y} = \frac{\partial u_x^{(0)}}{\partial z} = 0 \; ; \; div \; \overset{\leftrightarrow}{G}^{(iso)} = \frac{1}{4\pi(\lambda + 2\mu)}\vec{\nabla}\left(\frac{e^{-ik_\alpha R}}{R}\right)$$

$$\frac{\partial u_y^{(0)}}{\partial y} = -iu_0^p k_\alpha \sin^2\theta_0 \; ; \; \frac{\partial u_z^{(0)}}{\partial z} = -iu_0^p k_\alpha \cos^2\theta_0 \; ; \; div \; \vec{u}^{(0)} = -iu_0^p k_\alpha \qquad (2.11)$$

$$\frac{\partial u_y^{(0)}}{\partial x} = \frac{\partial u_z^{(0)}}{\partial x} = 0 \; ; \; \frac{\partial u_z^{(0)}}{\partial y} = \frac{\partial y_y^{(0)}}{\partial z} = -iu_0^p k_\alpha \sin\theta_0 \cos\theta_0 \; .$$

In the *far-field*, we obtain from Eq. (2.3), to terms of order $(k_\alpha R)^{-2}$

$$div \; \overset{\leftrightarrow}{G} = -\frac{ik_\alpha}{4\pi(\lambda + 2\mu)} \frac{e^{-ik_\alpha R}}{R}\vec{e}_R \; . \qquad (2.12)$$

Also,

$$\vec{e}_x\frac{\partial}{\partial x} = [\vec{e}_R \sin^2\theta\cos^2\phi + \vec{e}_\theta \sin\theta\cos\theta\cos^2\phi - \vec{e}_\phi \sin\theta\cos\phi\sin\phi]\frac{\partial}{\partial R} \; ,$$

$$\vec{e}_y\frac{\partial}{\partial y} = [\vec{e}_R \sin^2\theta\sin^2\phi + \vec{e}_\theta \sin\theta\cos\theta\sin^2\phi + \vec{e}_\phi \sin\theta\cos\phi\sin\phi]\frac{\partial}{\partial R} \; ,$$

$$\vec{e}_z\frac{\partial}{\partial z} = [\vec{e}_R \cos^2\theta - \vec{e}_\theta \sin\theta\cos\theta]\frac{\partial}{\partial R} \; ,$$

$$\vec{e}_x\frac{\partial}{\partial y} + \vec{e}_y\frac{\partial}{\partial x} = [\vec{e}_R \sin 2\phi\sin\theta + \vec{e}_\theta \sin 2\phi\cos\theta + \vec{e}_\phi \cos 2\phi]\sin\theta\frac{\partial}{\partial R} \; , \qquad (2.13)$$

$$\vec{e}_y\frac{\partial}{\partial z} + \vec{e}_z\frac{\partial}{\partial y} = [\vec{e}_R \sin 2\theta\sin\phi + \vec{e}_\theta \cos 2\theta\sin\phi + \vec{e}_\phi \cos\theta\cos\phi]\frac{\partial}{\partial R} \; ,$$

$$\vec{e}_z\frac{\partial}{\partial x} + \vec{e}_x\frac{\partial}{\partial z} = [\vec{e}_R \sin 2\theta\cos\phi + \vec{e}_\theta \cos 2\theta\cos\phi - \vec{e}_\phi \cos\theta\sin\phi]\frac{\partial}{\partial R} \; ,$$

where (R, θ, ϕ) are spherical coordinates of the observation point and $(\vec{e}_R, \vec{e}_\theta, \vec{e}_\phi)$ are the associated unit vectors (Fig. 1).

Using Eqs. (2.11)–(2.13), the final expressions for the spherical displacements compo-

53

nents, yielding the respective P, SV and SH wave motions, are

$$u_R = -U_0^{(p)} \frac{k_\alpha^2 (\delta v)}{4\pi} F_{RP}(\theta_0;\ \theta;\ \phi;\ C_{ij}) \frac{e^{i\omega\left(t-\frac{R}{\alpha}\right)}}{R} \tag{2.14}$$

$$u_\theta = U_0^{(p)} \frac{k_\alpha^2 (\delta v)}{4\pi} \frac{\alpha}{\beta}\ F_{\theta P}(\theta_0;\ \theta;\ \phi;\ C_{ij}) \frac{e^{i\omega\left(t-\frac{R}{\beta}\right)}}{R} \tag{2.15}$$

$$u_\phi = -U_0^{(p)} \frac{k_\alpha^2 (\delta v)}{4\pi} \frac{\alpha}{\beta}\ F_{\phi P}(\theta_0;\ \theta;\ \phi;\ C_{ij}) \frac{e^{i\omega\left(t-\frac{R}{\beta}\right)}}{R}\ . \tag{2.16}$$

The functions

$$F_{RP} = \frac{\delta C_{13}}{\lambda + 2\mu} + \frac{\delta C_{33} - \delta C_{13}}{\lambda + 2\mu} \cos^2\theta_0 \cos^2\theta + \frac{\delta C_{11} - \delta C_{13}}{\lambda + 2\mu} \sin^2\theta_0 \sin^2\theta$$

$$- 2\frac{\delta C_{66}}{\lambda + 2\mu} \sin^2\theta_0 \sin^2\theta \cos^2\phi + 2\frac{\delta C_{44}}{\lambda + 2\mu} \sin\theta_0 \cos\theta_0 \sin 2\theta \sin\phi \tag{2.17}$$

$$F_{\theta P} = \frac{\delta C_{33} - \delta C_{13}}{\mu} \cos^2\theta_0 \sin\theta \cos\theta - \frac{\delta C_{11} - \delta C_{13}}{\mu} \sin^2\theta_0 \sin\theta \cos\theta$$

$$+ 2\frac{\delta C_{66}}{\mu} \sin^2\theta_0 \sin\theta \cos\theta \cos^2\phi - 2\frac{\delta C_{44}}{\mu} \sin\theta_0 \cos\theta_0 \cos 2\theta \sin\phi \tag{2.18}$$

$$F_{\phi P} = \frac{\delta C_{66}}{\mu} \sin^2\theta_0 \sin\theta \sin 2\phi + \frac{\delta C_{44}}{\mu} \sin^2\theta_0 \cos\theta \cos\phi\ , \tag{2.19}$$

are the ensuing *radiation-patterns*. Figures 2-6 display three-dimensional amplitude patterns resulting from the interaction of the obstacle with an incident P-wave: $F_{RP}(\theta_0 = 0)$ in Figure 2; $F_{\theta P}(\theta_0 = 0)$ in Figure 3; $F_{RP}(\theta_0 = 90°)$ in Figure 4; $F_{\theta P}(\theta_0 = 90°)$ in Figure 5; $F_{\phi P}(\theta_0 = 90°)$ in Figure 6. Numerical values of the paramaters involved in the calculation

are given in Table 1.

(b) Incident SV-Wave $\left(\beta = \sqrt{\mu/\rho}\right)$

Let

$$\vec{u}^{(0)} = U_0^{(SV)}(\vec{e}_x \times \vec{p})e^{i\omega\left[t - \frac{1}{\beta}(y\sin\theta_0 + z\cos\theta_0)\right]} = u_0^{(SV)}(\vec{e}_x \times \vec{p}) , \qquad (2.20)$$

with the partial derivatives

$$u_x^{(0)} = 0 \;\; ; \;\; \frac{\partial u_x^{(0)}}{\partial x} = \frac{\partial u_x^{(0)}}{\partial y} = \frac{\partial u_x^{(0)}}{\partial z} = \frac{\partial u_y^{(0)}}{\partial x} = \frac{\partial u_z^{(0)}}{\partial x} = 0 ,$$

$$\frac{\partial u_y^{(0)}}{\partial y} = iu_0^{(SV)}k_\beta \sin\theta_0 \cos\theta_0 \;\; ; \;\; \frac{\partial u_y^{(0)}}{\partial z} = -iu_0^{(SV)}k_\beta \cos^2\theta_0 = \frac{\partial u_z^{(0)}}{\partial y} , \qquad (2.21)$$

$$\frac{\partial u_z^{(0)}}{\partial z} = -iu_0^{(SV)}k_\beta \sin\theta_0 \cos\theta_0 \;\; ; \;\; div\,\vec{u}^{(0)} = 0 .$$

The corresponding displacement components are:

$$u_R = -U_0^{(SV)}\frac{k_\beta^2(\delta v)}{4\pi}\frac{\beta}{\alpha}F_{R(SV)}(\theta_0;\,\theta;\,\phi;\,C_{ij})\frac{e^{i\omega\left(t - \frac{R}{\alpha}\right)}}{R} , \qquad (2.22)$$

$$u_\theta = U_0^{(SV)}\frac{k_\beta^2(\delta v)}{4\pi}F_{\theta(SV)}(\theta_0;\,\theta;\,\phi;\,C_{ij})\frac{e^{i\omega\left(t - \frac{R}{\beta}\right)}}{R} , \qquad (2.23)$$

$$u_\phi = U_0^{(SV)}\frac{k_\beta^2(\delta v)}{4\pi}F_{\phi(SV)}(\theta_0;\,\theta;\,\phi;\,C_{ij})\frac{e^{i\omega\left(t - \frac{R}{\beta}\right)}}{R} , \qquad (2.24)$$

where

$$F_{R(SV)} = \left[\frac{\delta C_{33} - \delta C_{13}}{\mu}\right]\sin\theta_0\cos\theta_0\cos^2\theta - \left[\frac{\delta C_{11} - \delta C_{13}}{\mu}\right]\sin\theta_0\cos\theta_0\sin^2\theta$$

$$+ \frac{\delta C_{66}}{\mu}\sin\theta_0\cos\theta_0\sin^2\theta\cos^2\phi - \frac{\delta C_{44}}{\mu}\cos2\theta_0\sin2\theta\sin\phi \qquad (2.25)$$

$$F_{\theta(SV)} = \left[\frac{\delta C_{33} - \delta C_{13}}{\mu} \right] \sin \theta_0 \cos \theta_0 \sin \theta \cos \theta + \left[\frac{\delta C_{11} - \delta C_{13}}{\mu} \right] \sin \theta_0 \cos \theta_0 \sin \theta \cos \theta$$

$$- \frac{\delta C_{66}}{\mu} \sin \theta_0 \cos \theta_0 \sin 2\theta \cos^2 \phi + \frac{\delta C_{44}}{\mu} \cos 2\theta_0 \cos 2\theta \sin \phi \qquad (2.26)$$

$$F_{\phi(SV)} = \frac{\delta C_{66}}{\mu} \sin \theta_0 \cos \theta_0 \sin \theta \sin 2\phi + \frac{\delta C_{44}}{\mu} \cos 2\theta_0 \cos \theta \cos \phi \qquad (2.27)$$

Figures 7–9 display three-dimensional amplitude patterns resulting from the interaction of the obstacle with the impinging SV wave: $F_{R(SV)}(\theta_0 = 0)$ in Figure 7; $F_{\theta(SV)}(\theta_0 = 0)$ in Figure 8; $F_{\phi(SV)}(\theta_0 = 0)$ in Figure 9. Numerical values of the participating parameters are shown in Table 1.

(c) Incident SH-wave $\left(\beta = \sqrt{\mu/\rho} \right)$

We take

$$\vec{u}^{(0)} = U_0^{(SH)} \vec{e}_x e^{i\omega \left[t - \frac{1}{\beta}(y \sin \theta_0 + z \cos \theta_0) \right]} = u_0^{(SH)} \vec{e}_x . \qquad (2.28)$$

Since the non-vanishing derivatives are

$$\frac{\partial u_x^{(0)}}{\partial y} = -i u_0^{(SH)} k_\beta \sin \theta_0 \quad ; \quad \frac{\partial u_x^{(0)}}{\partial z} = -i u_0^{(SH)} k_\beta \cos \theta_0 , \qquad (2.29)$$

only $\vec{u}_4^{(1)}$ and $\vec{u}_5^{(1)}$ in (2.7)–(2.8), survive. We then find that in this case

$$u_R = -U_0^{\prime(SH)}\frac{k_\beta^2(\delta v)}{4\pi}\frac{\beta}{\alpha}F_{R(SH)}(\theta_0;\ \theta;\ \phi;\ C_{ij})\frac{e^{-ik_\alpha R}}{R} \qquad (2.30)$$

$$u_\theta = -U_0^{(SH)}\frac{k_\beta^2(\delta v)}{4\pi}F_{\theta(SH)}(\theta_0;\ \theta;\ \phi;\ C_{ij})\frac{e^{-ik_\beta R}}{R} \qquad (2.31)$$

$$u_\phi = U_0^{(SH)}\frac{k_\beta^2(\delta v)}{4\pi}F_{\phi(SH)}(\theta_0;\ \theta;\ \phi;\ C_{ij})\frac{e^{-ik_\beta R}}{R} \qquad (2.32)$$

with

$$F_{R(SH)} = \frac{\delta C_{44}}{\mu}\cos\theta_0\sin 2\theta\cos\phi + \frac{\delta C_{66}}{\mu}\sin\theta_0\sin^2\theta\sin 2\phi \qquad (2.33)$$

$$F_{\theta(SH)} = \frac{\delta C_{44}}{\mu}\cos\theta_0\cos 2\theta\cos\phi + \frac{\delta C_{66}}{\mu}\sin\theta_0\cos\theta\sin\theta\sin 2\phi \qquad (2.34)$$

$$F_{\phi(SH)} = \frac{\delta C_{44}}{\mu}\cos\theta_0\cos\theta\sin\phi - \frac{\delta C_{66}}{\mu}\sin\theta_0\sin\theta\cos 2\phi \qquad (2.35)$$

Figures 10–12 show the radiation pattern resulting from the scattering of SH waves by the obstacle: $F_{R(SH)}(\theta_0 = 90°)$ in Figure 10; $F_{\theta(SH)}(\theta_0 = 90°)$ in Figure 11; $F_{\phi(SH)}(\theta_0 = 90°)$ in Figure 12.

3. EVALUATION OF THE ANISOTROPY COEFFICIENTS

The scattered field is governed by the nine elements of the *scattering matrix*

$$S = \begin{bmatrix} F_{RP} & F_{RSV} & F_{RSH} \\ F_{\theta P} & F_{\theta SV} & F_{\theta SH} \\ F_{\phi P} & F_{\phi SV} & F_{\phi SH} \end{bmatrix} . \tag{3.1}$$

These elements are functions of five independent material constants,

$$\delta_1 = \delta C_{13} ,$$

$$\delta_2 = \delta C_{33} - \delta C_{13} ,$$

$$\delta_3 = \delta C_{11} - \delta C_{13} , \tag{3.2}$$

$$\delta_4 = \delta C_{44} ,$$

$$\delta_5 = \delta C_{66} .$$

We shall prescribe six hypothetical experiments through which δC_{11}, δC_{33}, δC_{13}, δC_{44}, δC_{66} and θ_0 can be determined.

Experiment 1: Determination of the Symmetry Axis

We radiate the inclusion with a *plane P-wave* and observe the field along the direction of the wave normal $\vec{p}$ only, i.e.: at the point where $\theta = \pm\theta_0$. It is clear from Eqs. (2.17)–(2.19) that as we vary $\vec{p}$ on a unit sphere, there will be only one direction in space along which $F_{\theta P} = F_{\phi P} = 0$, $F_{RP} \neq 0$. This direction coincides with the symmetry axis, relative to which θ_0 and θ are measured and $\{SV, SH\}$ are defined.

Experiment 2: Determination of δC_{44}

Radiate the inclusion with a *plane SV wave* along $\theta_0 = 0$ and observe the field at $\theta = \theta_0 = 0$. Then via (2.25)–(2.27)

$$ F_{RSV} = 0 \quad , \quad F_{\theta SV} = -\frac{2\delta C_{44}}{\mu}\sin\phi \quad ; \quad F_{\phi SV} = \frac{2\delta C_{44}}{\mu}\cos\phi \, , \tag{3.3} $$

will yield (δC_{44}) for a given ϕ.

Experiment 3: Determination of δC_{66}

Radiate the inclusion with a *plane SH wave* along $\theta_0 = 90°$ and observe at $\theta = 90°$. Then via (2.33)–(2.35) we find

$$ F_{RSH} = \frac{\delta C_{66}}{\mu}\sin 2\phi \quad ; \quad F_{\theta SH} = 0 \quad , \quad F_{\phi SH} = -\frac{\delta C_{66}}{\mu}\cos 2\phi \, . \tag{3.4} $$

Experiment 4: Determination of δC_{13}

Radiate the inclusion with a *plane P-wave* at $\theta_0 = 0$ and observe the field at $\theta = 90°$. Then, via (2.17)–(2.19) we have

$$F_{RP} = \frac{\delta C_{13}}{\lambda + 2\mu} \quad ; \quad F_{\theta P} = 0 \quad , \quad F_{\phi P} = 0 .$$

Experiment 5: Determination of δC_{33}

Radiate the inclusion with a *plane P-wave* at $\theta_0 = 0$ and observe the field at $\theta = 0$. Then, via (2.17)–(2.19):

$$F_{RP} = \frac{\delta C_{33}}{\lambda + 2\mu} \quad ; \quad F_{\theta P} = 0 \quad ; \quad F_{\phi P} = 0 .$$

Experiment 6: Determination of δC_{11}

Radiate the inclusion with a *plane P-wave* at $\theta_0 = 90°$ and observe at $\theta = 90° \phi = 90°$. Then, via (2.17)–(2.19):

$$F_{RP} = \frac{\delta C_{11}}{\lambda + 2\mu} \quad ; \quad F_{\theta P} = 0 \quad ; \quad F_{\phi P} = 0 .$$

DISCUSSION

The theoretical results discussed above show the effect on elastic wave propagation of Rayleigh scattering due to azimuthally isotropic obstacles in an otherwise homogeneous medium. This effect may be important for the study of propagation of elastic waves in various materials. For example, the differences between the effects of azimuthally isotropic and isotropic scatterers can be considered. The radiation pattern corresponding to an isotropic obstacle will be the same as that presented in Figs. 2 and 4 for vertically incident P and SV signals on the azimuthally isotropic scatterer. As the angle of incidence θ_0 changes, the isotropic radiation patterns for scattered P and total S-waves will simply rotate along with the incident wave number vector, although there will be some interchange between SH and SV polarizations. Comparison of Figs. 2 and 3 shows that the radiation patterns for the azimuthally isotropic scatterer will actually change shape, depending on the relative magnitudes of the different perturbations to the elastic constants δC_{IJ}. The most important difference, however, is that since the scattering amplitudes for horizontal incidence depend on different elastic constants than for vertical incidence, the magnitude of backscattering may be significantly different for these two cases. On the other hand, for the isotropic case, the amplitude will remain the same.

A second area of importance for the scattering theory is in reference to theories for inversion of acoustic and seismic reflection data. An analysis of radiation patterns for point

61

diffractors by Tarantola (1986) shows that for an isotropic medium, an earth model is best parameterized in terms of S and P impedances and density in order to perform a general inversion for medium properties using nearly vertically propagating waves. Impedance for an anisotropic medium is a somewhat ill defined concept due to the directional variation of velocity, but if the impedance is defined using vertical velocities, the conclusions of Tarantola (1986) can still be applied to the azimuthally isotropic medium. The constant perturbations δC_{33} and δC_{44} would take the roles of $\delta\lambda$ and $\delta\mu$, respectively, in this case, since these are the constants affecting vertical propagation.

However, a determination of all 5 elastic parameters is desirable. While the list of hypothetical experiments in Section 3 shows that in principle all 5 constants are attainable through observations of scattering, it is also clear that a wide range of incidence angles relative to the axis of symmetry and three types of incident waves are required for the investigation. Therefore, experiments within the earth must consider both nearly vertically and nearly horizontally propagating signals, and a large data set must be obtained.

Although the application of these scattering concepts to inversion work will be difficult, they will still be important in understanding observations and forward modeling of propagation within a medium containing azimuthally isotropic inclusions, such as shale materials. The variation of the radiation patterns from the isotropic case may help to explain some unusual observations, such as anomalous S-wave signals in explosion data (e.g., Kisslinger

62

et al., 1961). Considering the prevalence of anisotropic media in many areas (Winterstein, 1986), inclusion of these effects is warranted.

REFERENCES

Ben-Menahem, A., 1989a, The elastodynamic Green's tensor and fields of point sources in anisotropic media, *Geophys. J. Royal Astro. Soc.*, submitted.

Ben-Menahem, A., 1989b, SH waves from point sources in anisotropic inhomogeneous media, *Geophysics,* submitted.

Ben-Menahem, A. and S.T. Singh, 1981, *Seismic Waves and Sources,* Springer Verlag, New York.

Gubernatis, J.E., Domany, E., Krumhansl, J.A., and M. Huberman, 1977, Born approximation in the theory of the scattering of elastic waves by flows, *J. Appl. Phys., 48,* 2812–2819.

Gupta, I.N. and R.R. Blandford, 1983, A mechanism for generation of short-period transverse motion from explosions, *Bull. Seism. Soc. Am., 73*, 571–591.

Haddon, R.A.W. and J.R. Cleary, 1974, Evidence for scattering of seismic PKP waves near the mantle-core boundary, *Phys. Earth and Planet. Int., 8,* 211–234.

Kisslinger, C., E.J. Mateker, Jr., and T.V. McEvilly, 1961, SH motion from explosions in soil, *Jour. geophys. Res., 66,* 3487–3496.

Tarantola, A., 1986, A strategy for nonlinear elastic inversion of seismic reflection data, *Geophysics, 51,* 1893–1903.

Tarantola, A., G. Jobert, D. Trezeguet and E. Denelle, 1988, The non–linear inversion of seismic waveforms can be performed either by time extrapolation or by depth extrapolation, *Geophysical Prospecting, 36,* 383–416.

Winterstein, D.F., 1986, Anisotropy effects in P-wave and SH-wave stacking velocities contain information on lithology, *Geophysics, 51,* 661-672.

Wu. R. and K. Aki, 1985, Scattering characteristics of elastic waves by elastic heterogeneity, *Geophysics, 50,* 582–595.

ACKNOWLEDGMENTS

Table I. Parameter values used to calculate the radiation patterns presented in Figures 2–12.

Parameter	Value	Dimensions
λ_0	22.05×10^{10}	$\text{dyn} \cdot \text{cm}^{-2}$
μ_0	35.97×10^{10}	$\text{dyn} \cdot \text{cm}^{-2}$
ρ	2.70	$\text{g} \cdot \text{cm}^{-3}$
$U_0\omega^2\delta v$	1.0×10^6	$\text{cm}^4 \cdot \text{sec}^{-2}$
δC_{11}	1.0×10^9	x
δC_{33}	2.0×10^9	x
δC_{13}	0.5×10^9	$\text{dyn} \cdot \text{cm}^{-2}$
δC_{44}	1.0×10^9	x
δC_{66}	2.0×10^9	x
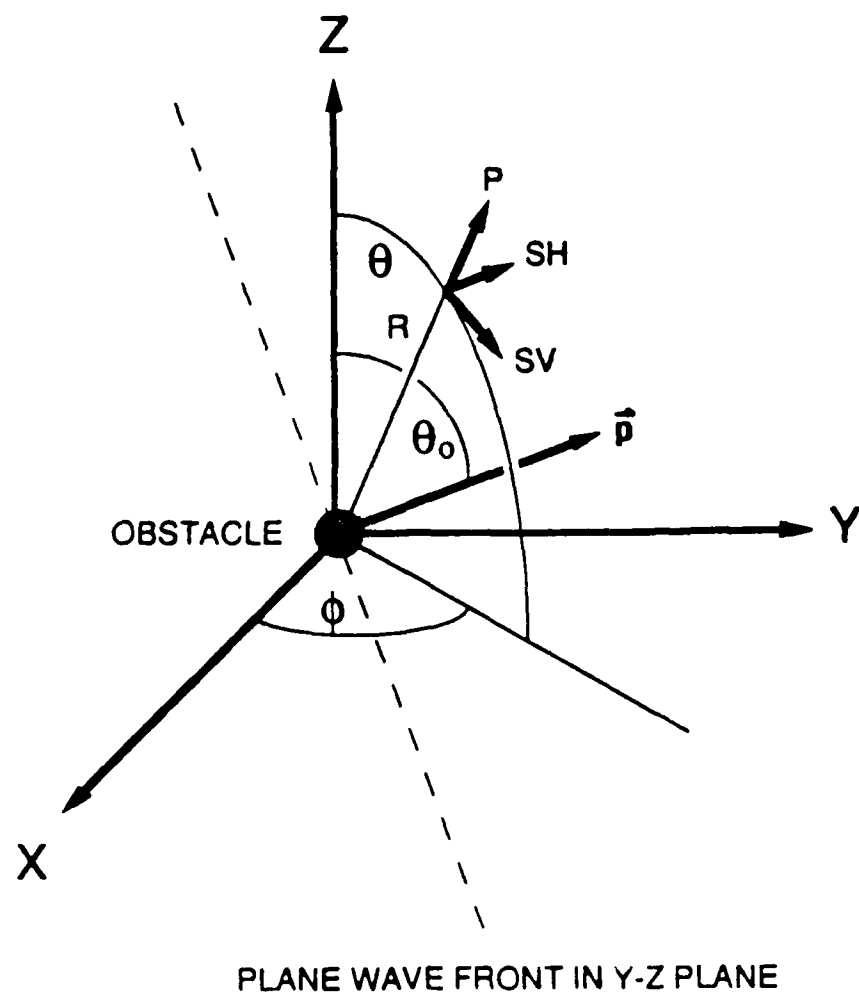
Figure 1: Coordinate system used to develop the expressions for the radiation patterns. The plane

wave, P or S, is assumed to be incident with a wave normal vector $\vec{p}$ in the $y - z$ plane.
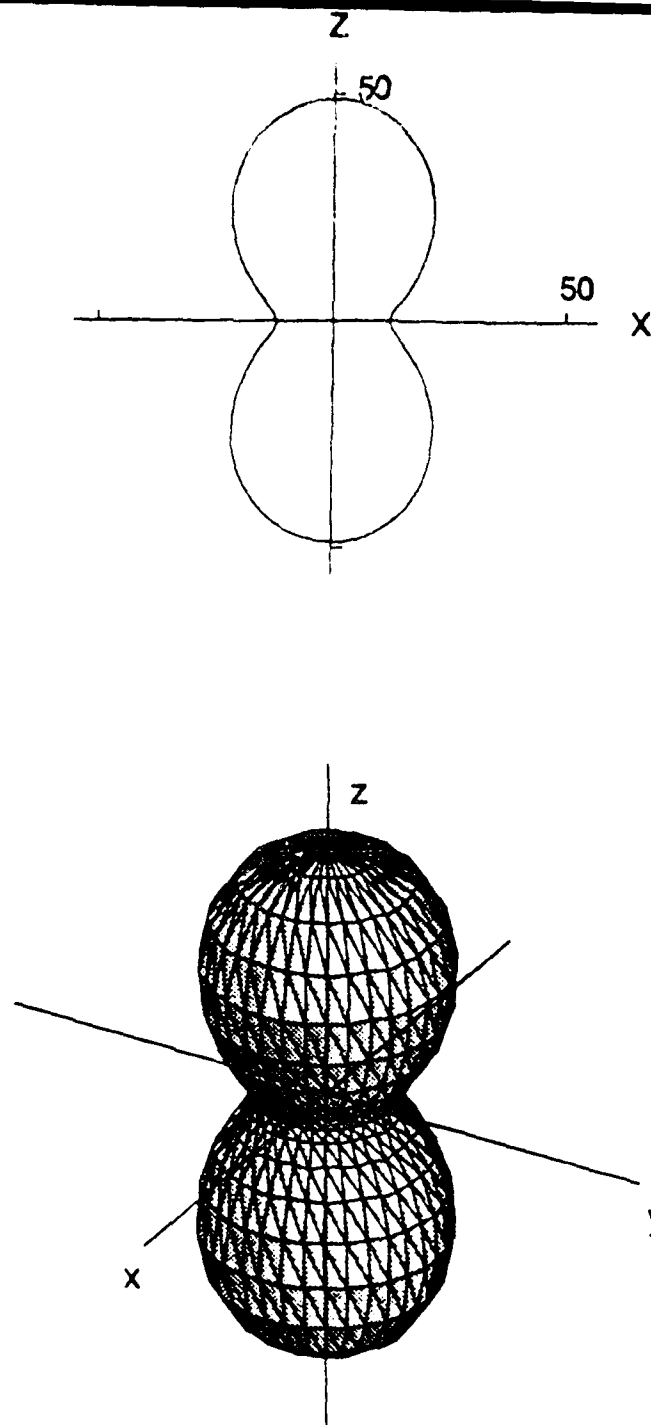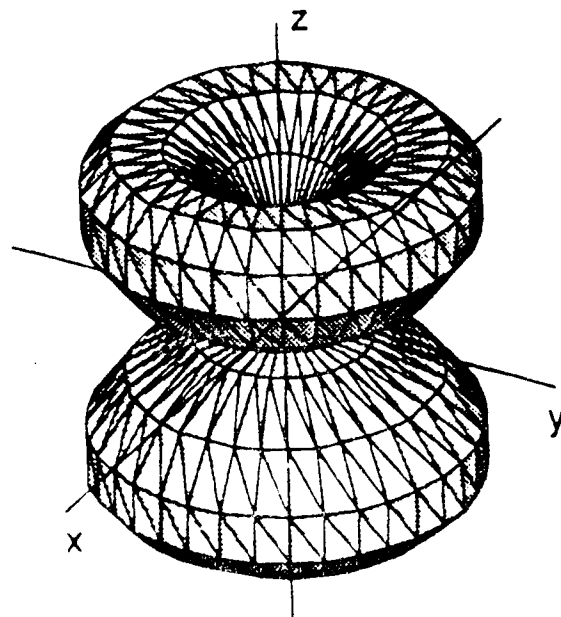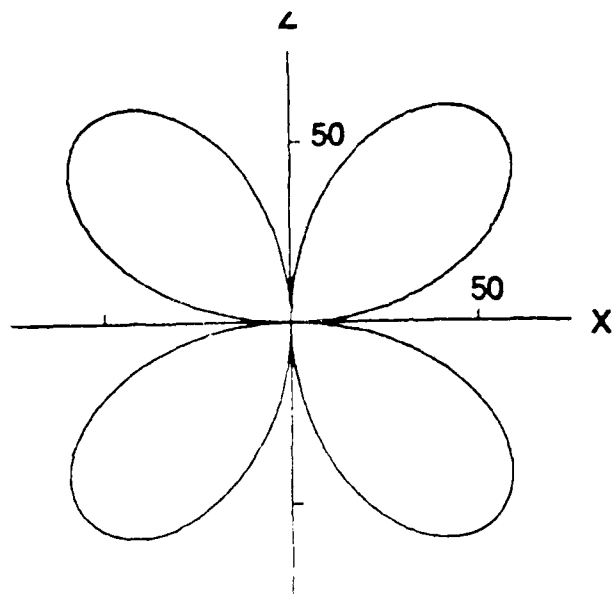
Figure 2: Radiation pattern for scattered P-waves generated by a P-wave incident along the symmetry axis ($\theta_0 = 0°$) for the parameter values given in Table 1. The upper portion of the figure shows a vertical cross-section of the radiation pattern in the $x - z$ plane, while the lower portion shows a perspective of the radiation in three dimensions. For this incidence angle, the radiation has rotational symmetry about the z-axis.

Figure 3: Radiation pattern for scattered SV-waves generated by a P-wave incident along the symmetry axis ($\theta_0 = 0^\circ$). The medium parameters are given in Table 1. The upper portion shows a vertical cross-section of the radiation pattern, and the lower portion shows a perspective of the radiation in three dimensions.
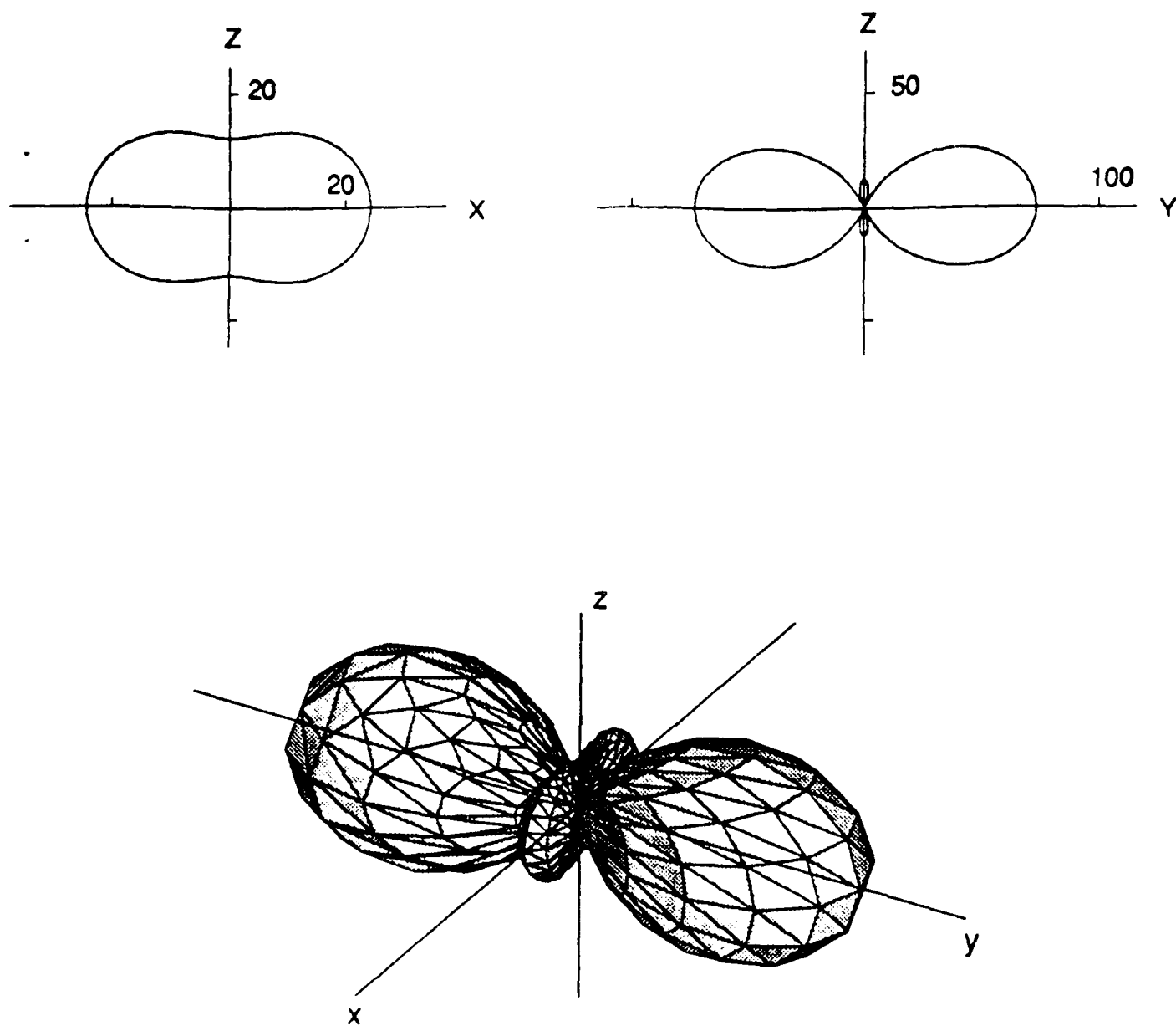
Figure 4: Radiation pattern for scattered P-waves due to a horizontally incident P-wave ($\theta_0 = 90°$) for the medium parameters indicated in Table 1. The upper portion shows vertical cross sections with the given orientations, and the lower part of the figure shows the three-dimensional perspective drawing of the radiation pattern.
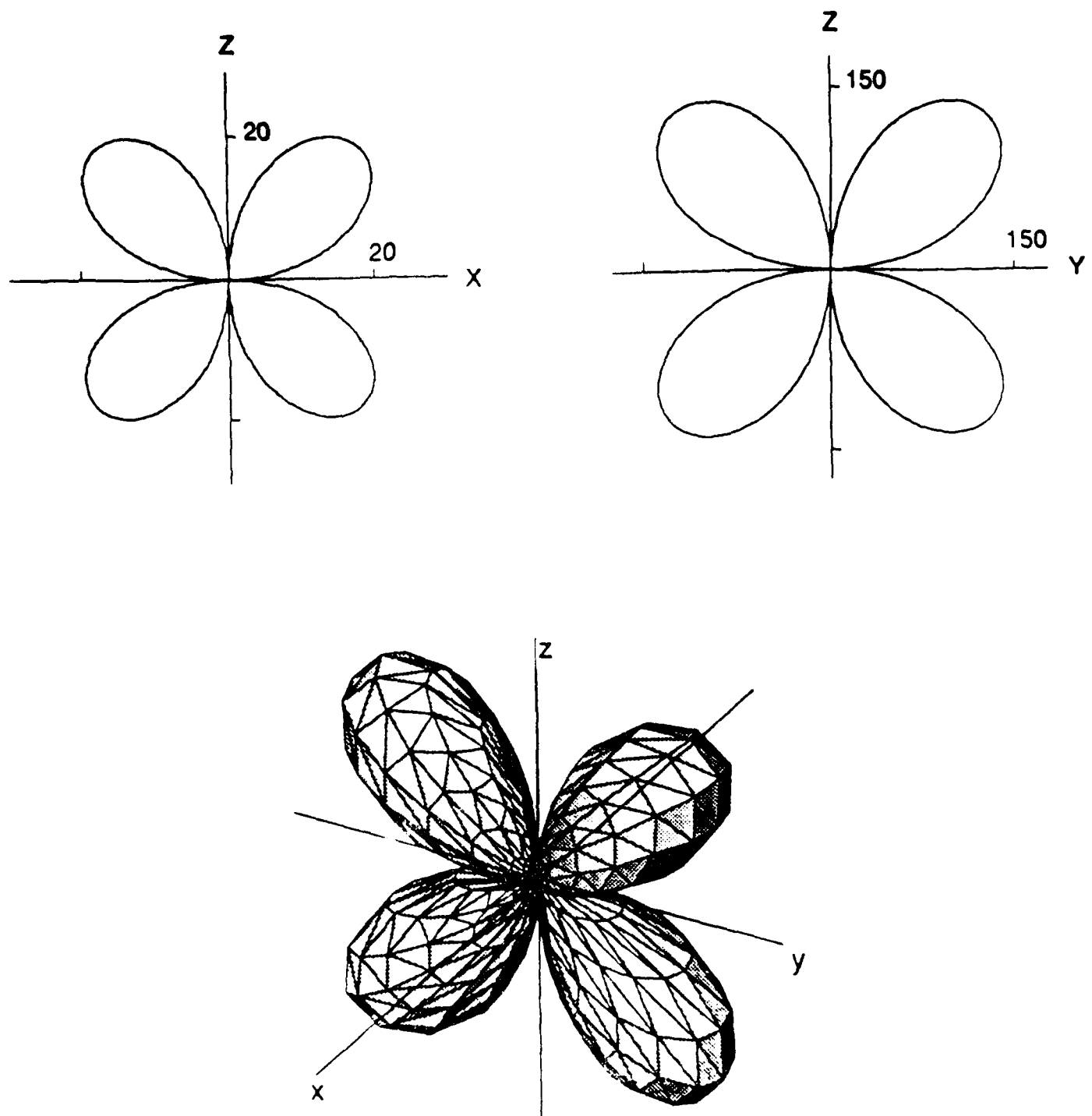
Figure 5: Radiation pattern for scattered SH-waves due to a horizontally incident P-wave ($\theta_0 = 90°$) for the parameter values given in Table 1. The format is the same as for Fig. 4.

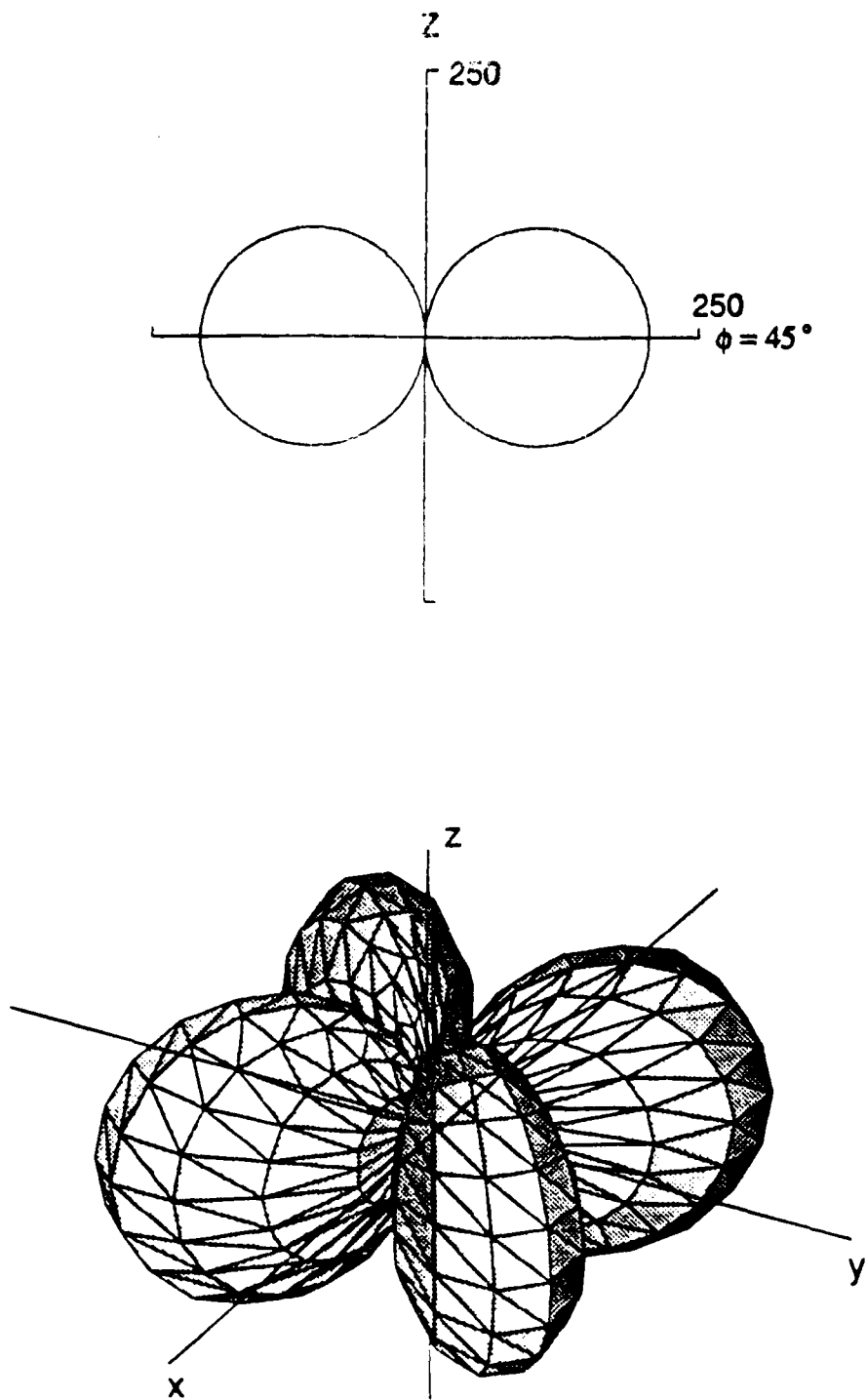Figure 6: Radiation pattern for scattered SH-waves due to a horizontally incident P-wave ($\theta_0 = 90°$) for the parameter values given in Table 1. The format is the same as for Fig. 4.

Figure 7: Radiation pattern for scattered P-waves due to a vertically incident SV-wave ($\theta_0 = 0°$) for the parameter values given in Table 1. The format is the same as for Fig. 4.
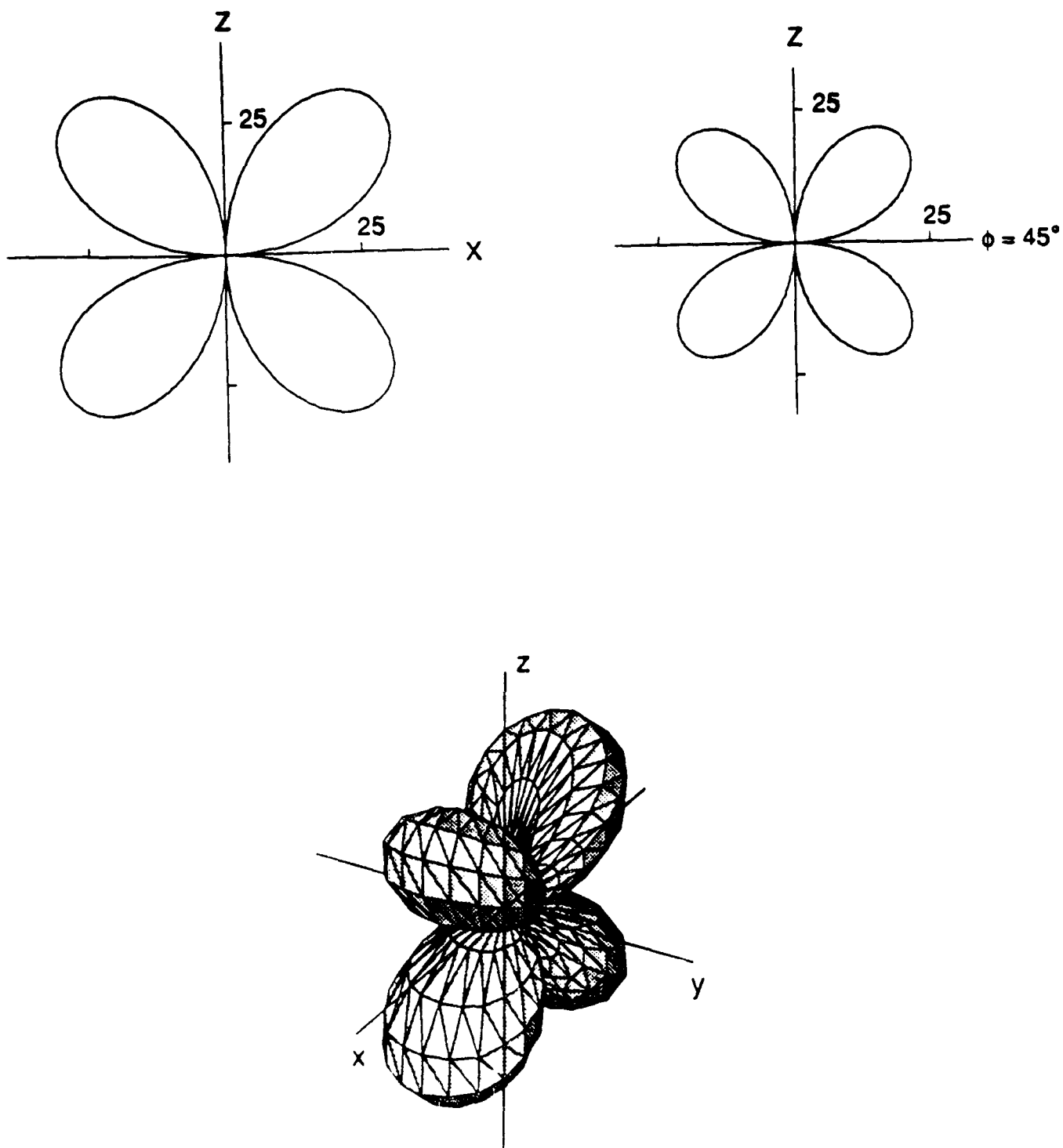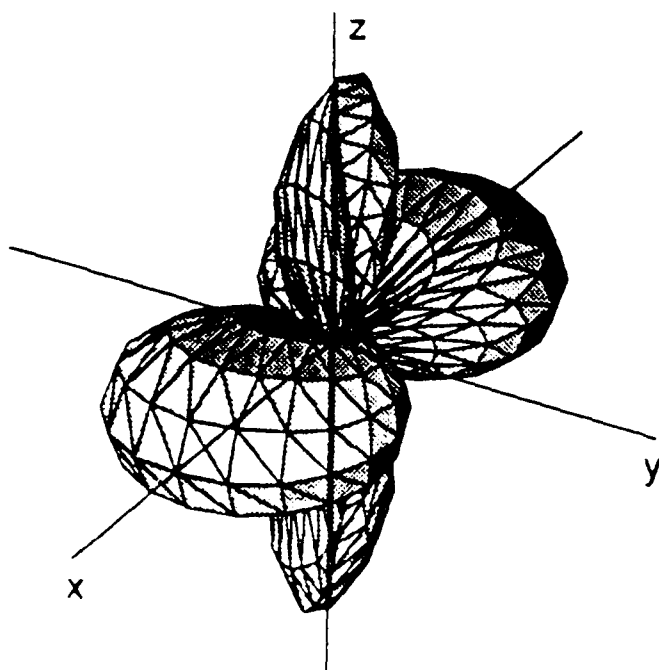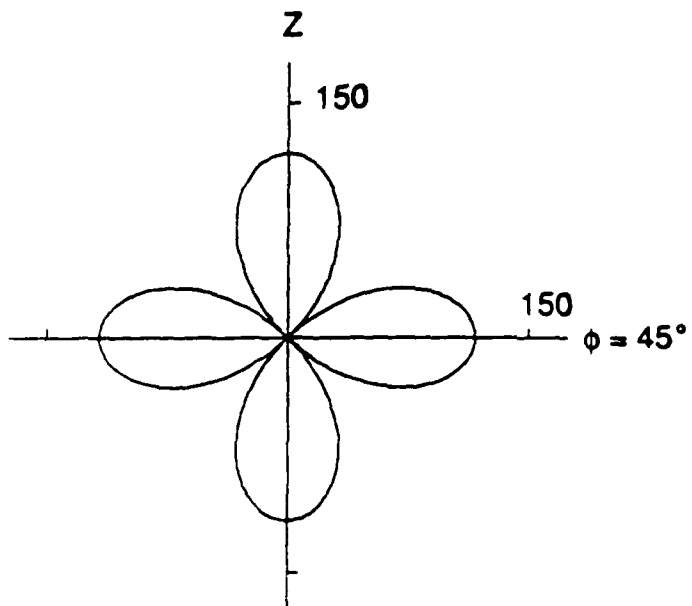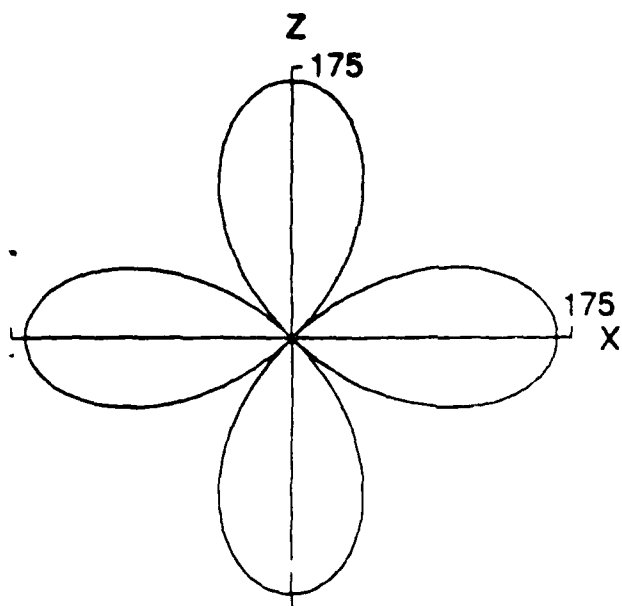
Figure 8: Radiation pattern for scattered SV-waves due to a vertically incident SV-wave ($\theta_0 = 0^\circ$) for the parameter values given in Table 1. The format is the same as for Fig. 4.
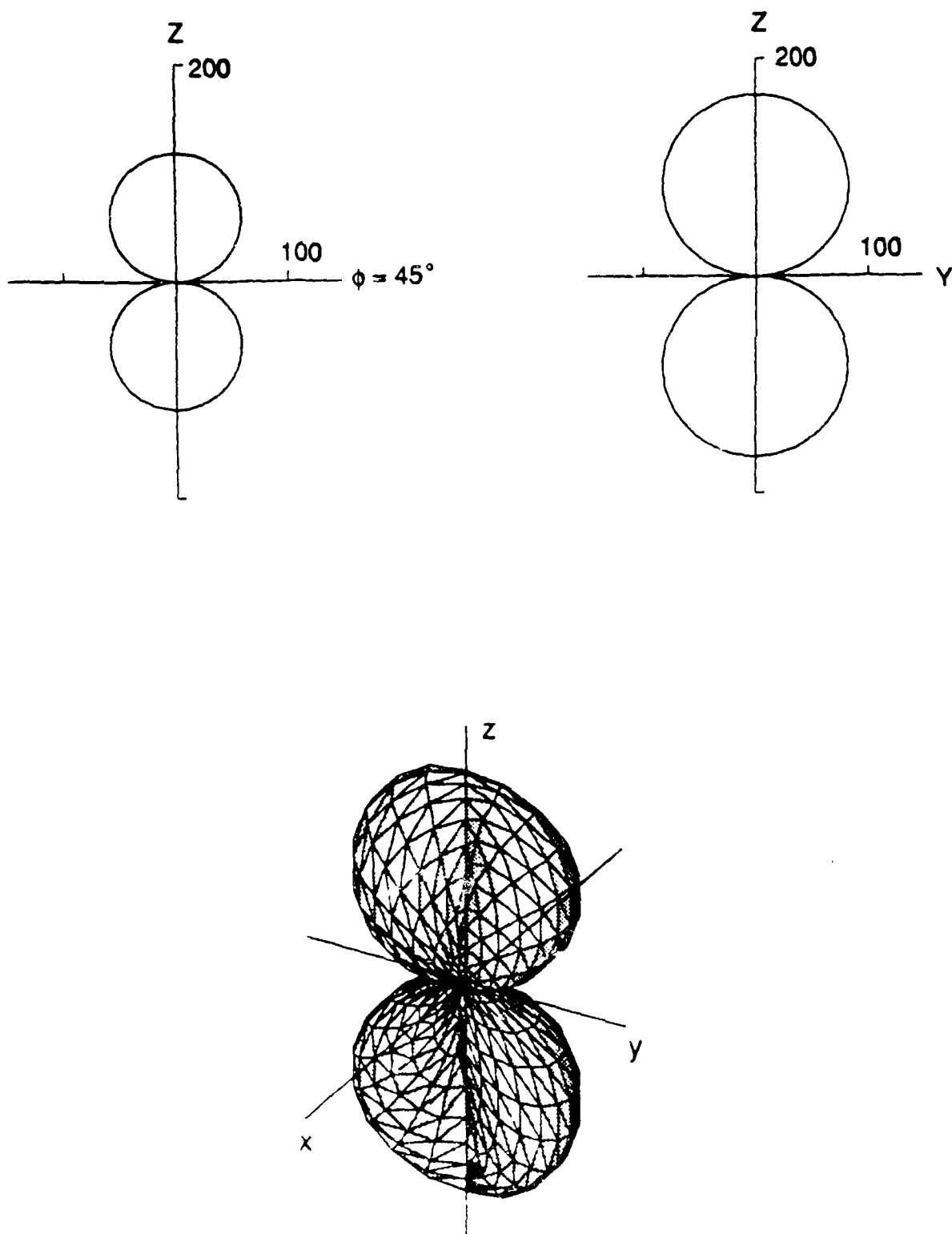
Figure 9: Radiation pattern for scattered SH-waves due to a vertically incident SV-wave $(\theta_0 = 0)$ for the parameter values given in Table 1. The format is the same as for Fig. 4.
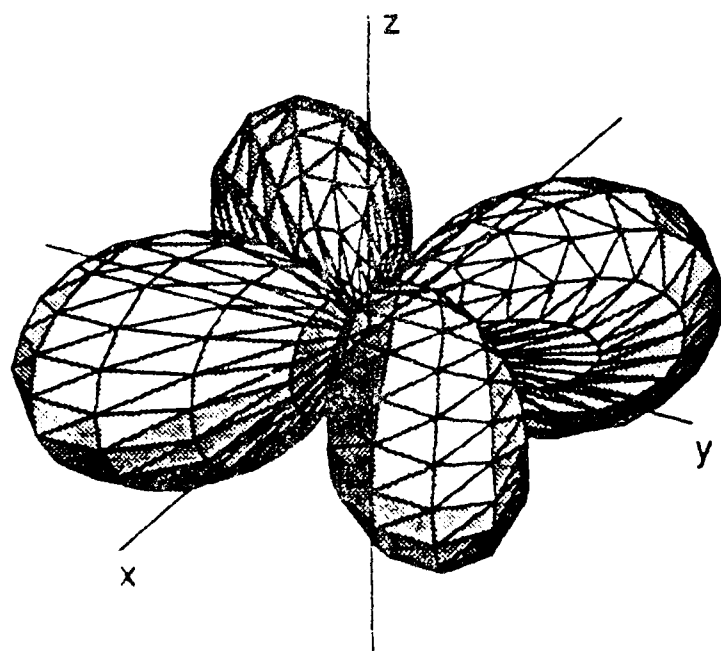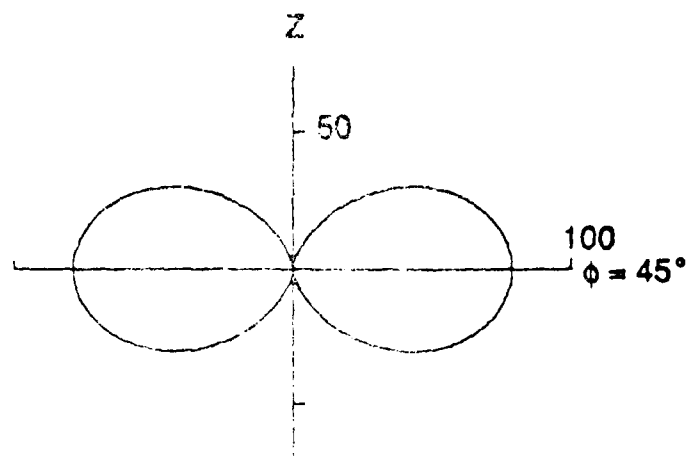
Figure 10: Radiation pattern for scattered P-waves due to a horizontally incident SH-wave ($\theta_0 = 90°$) for the parameter values given in Table 1. The format is the same as for Fig. 4.

Z

⌐ 150

150
φ = 45°

z

y

x

Figure 11: Radiation pattern for scattered SV-waves due to a horizontally incident SH-wave ($\theta_0 = 90°$) for the parameter values given in Table 1. The format is the same as for Fig. 1.

Figure 12: Radiation pattern for scattered SH-waves due to a horizontally incident SH-wave ($\theta_0 = 90°$) for the parameter values given in Table 1. The format is the same as for Fig. 4.
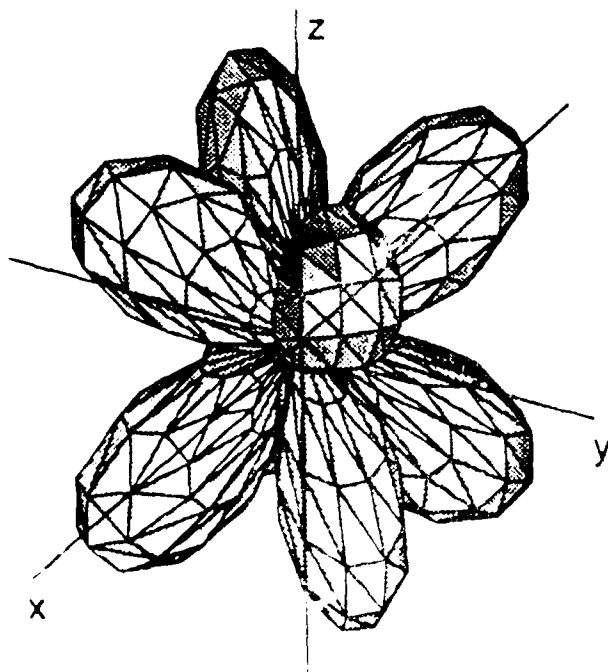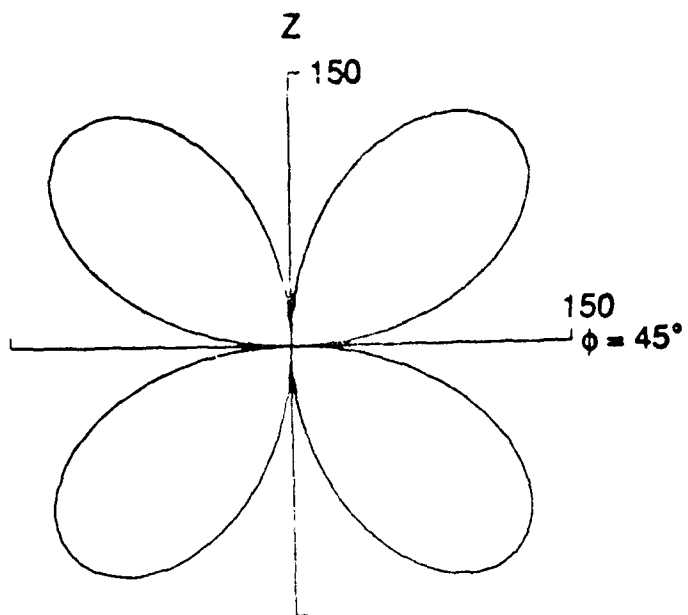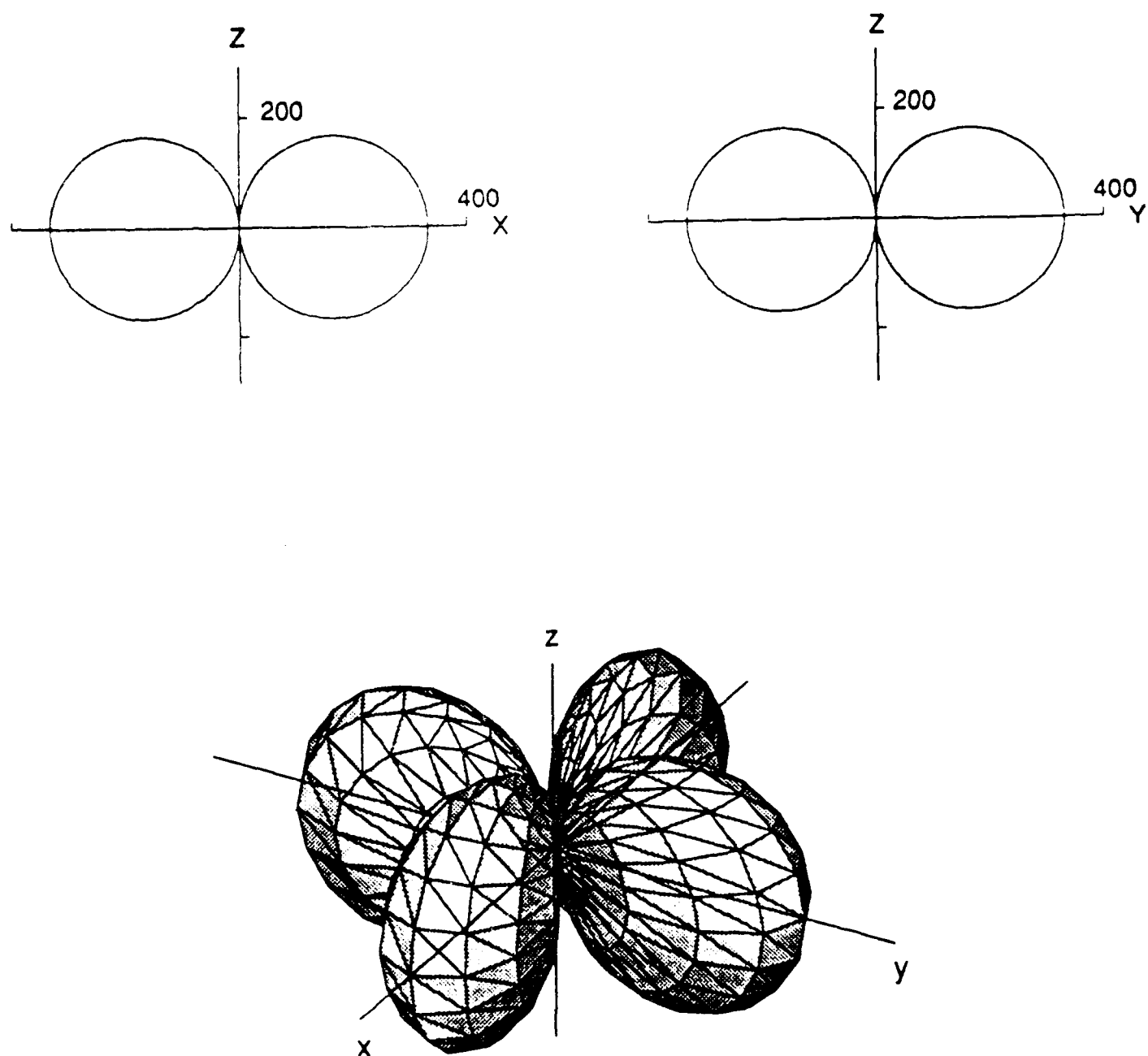
Prof. Thomas Ahrens
Seismological Lab, 252-21
Division of Geological & Planetary Sciences
California Institute of Technology
Pasadena, CA 91125

Prof. Charles B. Archambeau
CIRES
University of Colorado
Boulder, CO 80309

Prof. Muawia Barazangi
Institute for the Study of the Continent
Cornell University
Ithaca, NY 14853

Dr. Douglas R. Baumgardt
ENSCO, Inc
5400 Port Royal Road
Springfield, VA 22151-2388

Prof. Jonathan Berger
IGPP, A-025
Scripps Institution of Oceanography
University of California, San Diego
La Jolla, CA 92093

Dr. Lawrence J. Burdick
Woodward-Clyde Consultants
566 El Dorado Street
Pasadena, CA 91109-3245

Dr. Karl Coyner
New England Research, Inc.
76 Olcott Drive
White River Junction, VT 05001

Prof. Vernon F. Cormier
Department of Geology & Geophysics
U-45, Room 207
The University of Connecticut
Storrs, CT 06268

Prof. Steven Day
Department of Geological Sciences
San Diego State University
San Diego, CA 92182

Dr. Zoltan A. Der
ENSCO, Inc.
5400 Port Royal Road
Springfield, VA 22151-2388

Prof. John Ferguson
Center for Lithospheric Studies
The University of Texas at Dallas
P.O. Box 830688
Richardson, TX 75083-0688

Prof. Stanley Flatte
Applied Sciences Building
University of California
Santa Cruz, CA 95064

Dr. Alexander Florence
SRI International
333 Ravenswood Avenue
Menlo Park, CA 94025-3493

Prof. Henry L. Gray
Vice Provost and Dean
Department of Statistical Sciences
Southern Methodist University
Dallas, TX 75275

Dr. Indra Gupta
Teledyne Geotech
314 Montgomery Street
Alexandria, VA 22314

Prof. David G. Harkrider
Seismological Laboratory
Division of Geological & Planetary Sciences
California Institute of Technology
Pasadena, CA 91125

Prof. Donald V. Helmberger
Seismological Laboratory
Division of Geological & Planetary Sciences
California Institute of Technology
Pasadena, CA 91125

Prof. Eugene Herrin
Institute for the Study of Earth and Man
GeophysicalLaboratory
Southern Methodist University
Dallas, TX 75275

Prof . Robert B. Herrmann
Department of Earth & Atmospheric Sciences
St. Louis University
St. Louis, MO 63156

Prof. Bryan Isacks
Cornell University
Department of Geological Sciences
SNEE Hall
Ithaca, NY 14850

Dr. Rong-Song Jih
Teledyne Geotech
314 Montgomery Street
Alexandria, VA 22314

Prof. Lane R. Johnson
Seismographic Station
University of California
Berkeley, CA 94720

Prof. Alan Kafka
Department of Geology & Geophysics
Boston College
Chestnut Hill, MA 02167

Prof. Fred K. Lamb
University of Illinois at Urbana-Champaign
Department of Physics
1110 West Green Street
Urbana, IL 61801

Prof. Charles A. Langston
Geosciences Department
403 Deike Building
The Pennsylvania State University
University Park, PA 16802

Prof. Thorne Lay
Department of Geological Sciences
1006 C C. Little Building
University of Michigan
Ann Arbor, MI 48109-1063

Prof. Arthur Lerner-Lam
Lamont-Doherty Geological Observatory
of Columbia University
Palisades, NY 10964

Dr. Christopher Lynnes
Teledyne Geotech
314 Montgomery Street
Alexandria, VA 22314

Prof. Peter Malin
University of California at Santa Barbara
Institute for Crustal Studies
Santa Barbara, CA 93106

Dr. Randolph Martin, III
New England Research, Inc.
76 Olcott Drive
White River Junction, VT 05001

Dr. Gary McCartor
Mission Research Corporation
735 State Street
P.O. Drawer 719
Santa Barbara, CA 93102 (2 copies)

Prof. Thomas V. McEvilly
Seismographic Station
University of California
Berkeley, CA 94720

Dr. Keith L. McLaughlin
S-CUBED
A Division of Maxwell Laboratory
P.O. Box 1620
La Jolla, CA 92038-1620

Prof. William Menke
Lamont-Doherty Geological Observatory
of Columbia University
Palisades, NY 10964

Stephen Miller
SRI International
333 Ravenswood Avenue
Box AF 116
Menlo Park, CA 94025-3493

Prof. Bernard Minster
IGPP, A-025
Scripps Institute of Oceanography
University of California, San Diego
La Jolla, CA 92093

Prof. Brian J. Mitchell
Department of Earth & Atmospheric Sciences
St. Louis University
St. Louis, MO 63156

Mr. Jack Murphy
S-CUBED, A Division of Maxwell Laboratory
11800 Sunrise Valley Drive
Suite 1212
Reston, VA 22091 (2 copies)

Dr. Bao Nguyen
GL/LWH
Hanscom AFB, MA 01731-5000

Prof. John A. Orcutt
IGPP, A-025
Scripps Institute of Oceanography
University of California, San Diego
La Jolla, CA 92093

Prof. Keith Priestley
University of Nevada
Mackay School of Mines
Reno, NV 89557

Prof. Paul G. Richards
Lamont-Doherty Geological Observatory
of Columbia University
Palisades, NY 10964

Dr. Wilmer Rivers
Teledyne Geotech
314 Montgomery Street
Alexandria, VA 22314

Dr. Alan S. Ryall, Jr.
Center for Seismic Studies
1300 North 17th Street
Suite 1450
Arlington, VA 22209-2308

Prof. Charles G. Sammis
Center for Earth Sciences
University of Southern California
University Park
Los Angeles, CA 90089-0741

Prof. Christopher H. Scholz
Lamont-Doherty Geological Observatory
of Columbia University
Palisades, NY 10964

Prof. David G. Simpson
Lamont-Doherty Geological Observatory
of Columbia University
Palisades, NY 10964

Dr. Jeffrey Stevens
S-CUBED
A Division of Maxwell Laboratory
P.O. Box 1620
La Jolla, CA 92038-1620

Prof. Brian Stump
Institute for the Study of Earth & Man
Geophysical Laboratory
Southern Methodist University
Dallas, TX 75275

Prof. Jeremiah Sullivan
University of Illinois at Urbana-Champaign
Department of Physics
1110 West Green Street
Urbana, IL 61801

Prof. Clifford Thurber
University of Wisconsin-Madison
Department of Geology & Geophysics
1215 West Dayton Street
Madison, WS 53706

Prof. M. Nafi Toksoz
Earth Resources Lab
Massachusetts Institute of Technology
42 Carleton Street
Cambridge, MA 02142

Prof. John E. Vidale
University of California at Santa Cruz
Seismological Laboratory
Santa Cruz, CA 95064

Prof. Terry C. Wallace
Department of Geosciences
Building #77
University of Arizona
Tucson, AZ 85721

Dr. Raymond Willeman
GL/LWH
Hanscom AFB, MA 01731-5000

Dr. Lorraine Wolf
GL/LWH
Hanscom AFB, MA 01731-5000

Prof. Francis T. Wu
Department of Geological Sciences
State University of New York
at Binghamton
Vestal, NY 13901

Dr. Monem Abdel-Gawad
Rockwell International Science Center
1049 Camino Dos Rios
Thousand Oaks, CA 91360

Prof. Keiiti Aki
Center for Earth Sciences
University of Southern California
University Park
Los Angeles, CA 90089-0741

Prof. Shelton S. Alexander
Geosciences Department
403 Deike Building
The Pennsylvania State University
University Park, PA 16802

Dr. Ralph Archuleta
Department of Geological Sciences
University of California at Santa Barbara
Santa Barbara, CA 93102

Dr. Thomas C. Bache, Jr.
Science Applications Int'l Corp.
10210 Campus Point Drive
San Diego, CA 92121 (2 copies)

J. Barker
Department of Geological Sciences
State University of New York
at Binghamton
Vestal, NY 13901

Dr. T.J. Bennett
S-CUBED
A Division of Maxwell Laboratory
11800 Sunrise Valley Drive, Suite 1212
Reston, VA 22091

Mr. William J. Best
907 Westwood Drive
Vienna, VA 22180

Dr. N. Biswas
Geophysical Institute
University of Alaska
Fairbanks, AK 99701

Dr. G.A. Bollinger
Department of Geological Sciences
Virginia Polytechnical Institute
21044 Derring Hall
Blacksburg, VA 24061

Dr. Stephen Bratt
Science Applications Int'l Corp.
10210 Campus Point Drive
San Diego, CA 92121

Michael Browne
Teledyne Geotech
3401 Shiloh Road
Garland, TX 75041

Mr. Roy Burger
1221 Serry Road
Schenectady, NY 12309

Dr. Robert Burridge
Schlumberger-Doll Research Center
Old Quarry Road
Ridgefield, CT 06877

Dr. Jerry Carter
Rondout Associates
P.O. Box 224
Stone Ridge, NY 12484

Dr. W. Winston Chan
Teledyne Geotech
314 Montgomery Street
Alexandria, VA 22314-1581

Dr. Theodore Cherry
Science Horizons, Inc.
710 Encinitas Blvd., Suite 200
Encinitas, CA 92024 (2 copies)

Prof. Jon F. Claerbout
Department of Geophysics
Stanford University
Stanford, CA 94305

Prof. Robert W. Clayton
Seismological Laboratory
Division of Geological & Planetary Sciences
California Institute of Technology
Pasadena, CA 91125

Prof. F. A. Dahlen
Geological and Geophysical Sciences
Princeton University
Princeton, NJ 08544-0676

-4-

Prof. Anton W. Dainty
Earth Resources Lab
Massachusetts Institute of Technology
42 Carleton Street
Cambridge, MA 02142

Prof. Adam Dziewonski
Hoffman Laboratory
Harvard University
20 Oxford St
Cambridge, MA 02138

Prof. John Ebel
Department of Geology & Geophysics
Boston College
Chestnut Hill, MA 02167

Eric Fielding
SNEE Hall
INSTOC
Cornell University
Ithaca, NY 14853

Prof. Donald Forsyth
Department of Geological Sciences
Brown University
Providence, RI 02912

Prof. Art Frankel
Mail Stop 922
Geological Survey
790 National Center
Reston, VA 22092

Dr. Anthony Gangi
Texas A&M University
Department of Geophysics
College Station, TX 77843

Dr. Freeman Gilbert
Inst. of Geophysics & Planetary Physics
University of California, San Diego
P.O. Box 109
La Jolla, CA 92037

Mr. Edward Giller
Pacific Sierra Research Corp.
1401 Wilson Boulevard
Arlington, VA 22209

Dr. Jeffrey W. Given
Sierra Geophysics
11255 Kirkland Way
Kirkland, WA 98033

Prof. Stephen Grand
University of Texas at Austin
Department of Geological Sciences
Austin, TX 78713-7909

Prof. Roy Greenfield
Geosciences Department
403 Deike Building
The Pennsylvania State University
University Park, PA 16802

Dan N. Hagedorn
Battelle
Pacific Northwest Laboratories
Battelle Boulevard
Richland, WA 99352

Kevin Hutchenson
Department of Earth Sciences
St. Louis University
3507 Laclede
St. Louis, MO 63103

Prof. Thomas H. Jordan
Department of Earth, Atmospheric
  and Planetary Sciences
Massachusetts Institute of Technology
Cambridge, MA 02139

Robert C. Kemerait
ENSCO, Inc.
445 Pineda Court
Melbourne, FL 32940

William Kikendall
Teledyne Geotech
3401 Shiloh Road
Garland, TX 75041

Prof. Leon Knopoff
University of California
Institute of Geophysics & Planetary Physics
Los Angeles, CA 90024

Prof. L. Timothy Long
School of Geophysical Sciences
Georgia Institute of Technology
Atlanta, GA 30332

Prof. Art McGarr
Mail Stop 977
Geological Survey
345 Middlefield Rd.
Menlo Park, CA 94025

Dr. George Mellman
Sierra Geophysics
11255 Kirkland Way
Kirkland, WA 98033

Prof. John Nabelek
College of Oceanography
Oregon State University
Corvallis, OR 97331

Prof. Geza Nagy
University of California, San Diego
Department of Ames, M.S. B-010
La Jolla, CA 92093

Prof. Amos Nur
Department of Geophysics
Stanford University
Stanford, CA 94305

Prof. Jack Oliver
Department of Geology
Cornell University
Ithaca, NY 14850

Prof. Robert Phinney
Geological & Geophysical Sciences
Princeton University
Princeton, NJ 08544-0636

Dr. Paul Pomeroy
Rondout Associates
P.O. Box 224
Stone Ridge, NY 12484

Dr. Jay Pulli
RADIX System, Inc.
2 Taft Court, Suite 203
Rockville, MD 20850

Dr. Norton Rimer
S-CUBED
A Division of Maxwell Laboratory
P.O. Box 1620
La Jolla, CA 92038-1620

Prof. Larry J. Ruff
Department of Geological Sciences
1006 C.C. Little Building
University of Michigan
Ann Arbor, MI 48109-1063

Dr. Richard Sailor
TASC Inc.
55 Walkers Brook Drive
Reading, MA 01867

Thomas J. Sereno, Jr.
Science Application Int'l Corp.
10210 Campus Point Drive
San Diego, CA 92121

John Sherwin
Teledyne Geotech
3401 Shiloh Road
Garland, TX 75041

Prof. Robert Smith
Department of Geophysics
University of Utah
1400 East 2nd South
Salt Lake City, UT 84112

Prof. S. W. Smith
Geophysics Program
University of Washington
Seattle, WA 98195

Dr. Stewart Smith
IRIS Inc.
1616 North Fort Myer Drive
Suite 1440
Arlington, VA 22209

Dr. George Sutton
Rondout Associates
P.O. Box 224
Stone Ridge, NY 12484

Prof. L. Sykes
Lamont-Doherty Geological Observatory
of Columbia University
Palisades, NY 10964

Prof. Pradeep Talwani
Department of Geological Sciences
University of South Carolina
Columbia, SC 29208

Prof. Ta-liang Teng
Center for Earth Sciences
University of Southern California
University Park
Los Angeles, CA 90089-0741

Dr. R.B. Tittmann
Rockwell International Science Center
1049 Camino Dos Rios
P.O. Box 1085
Thousand Oaks, CA 91360

Dr. Gregory van der Vink
IRIS, Inc.
1616 North Fort Myer Drive
Suite 1440
Arlington, VA 22209

William R. Walter
Seismological Laboratory
University of Nevada
Reno, NV 89557

Dr. Gregory Wojcik
Weidlinger Associates
4410 El Camino Real
Suite 110
Los Altos, CA 94022

Prof. John H. Woodhouse
Hoffman Laboratory
Harvard University
20 Oxford Street
Cambridge, MA 02138

Dr. Gregory B. Young
ENSCO, Inc.
5400 Port Royal Road
Springfield, VA 22151-2388

Dr. Ralph Alewine III
DARPA/NMRO
1400 Wilson Boulevard
Arlington, VA 01731-5000

Paul Johnson
ESS-4, Mail Stop J979
Los Alamos National Laboratory
Los Alamos, NM 87545

Mr. James C. Battis
GL/LWH
Hanscom AFB, MA 22209-2308

Janet Johnston
GL/LWH
Hanscom AFB, MA 01731-5000

Dr. Robert Blandford
DARPA/NMRO
1400 Wilson Boulevard
Arlington, VA 87185

Dr. Katharine Kadinsky-Cade
GL/LWH
Hanscom AFB, MA 01731-5000

Eric Chael
Division 9241
Sandia Laboratory
Albuquerque, NM 01731-5000

Ms. Ann Kerr
IGPP, A-025
Scripps Institute of Oceanography
University of California, San Diego
La Jolla, CA 92093

Dr. John J. Cipar
GL/LWH
Hanscom AFB, MA 01731-5000

Dr. Max Koontz
US Dept of Energy/DP 5
Forrestal Building
1000 Independence Avenue
Washington, DC 20585

Mr. Jeff Duncan
Office of Congressman Markey
2133 Rayburn House Bldg.
Washington, D.C. 20515

Dr. W.H.K. Lee
Office of Earthquakes, Volcanoes,
& Engineering
345 Middlefield Road
Menlo Park, CA 94025

Dr. Jack Evernden
USGS - Earthquake Studies
345 Middlefield Road
Menlo Park, CA 94025

Dr. William Leith
U.S. Geological Survey
Mail Stop 928
Reston, VA 22092

Art Frankel
USGS
922 National Center
Reston, VA 22092

Dr. Richard Lewis
Director, Earthquake Engineering & Geophysics
U.S. Army Corps of Engineers
Box 631
Vicksburg, MS 39180

Dr. T. Hanks
USGS
Nat'l Earthquake Research Center
345 Middlefield Road
Menlo Park, CA 94025

James F. Lewkowicz
GL/LWH
Hanscom AFB, MA 01731-5000

Dr. James Hannon
Lawrence Livermore Nat'l Laboratory
P.O. Box 808
Livermore, CA 94550

Mr. Alfred Lieberman
ACDA/VI-OA'State Department Bldg
Room 5726
320 - 21st Street, NW
Washington, DC 20451

Stephen Mangino
GL/LWH
Hanscom AFB, MA 01731-5000

Dr. Frank F. Pilotte
HQ AFTAC/TT
Patrick AFB, FL 32925-6001

Dr. Robert Masse
Box 25046, Mail Stop 967
Denver Federal Center
Denver, CO 80225

Katie Poley
CIA-OSWR/NED
Washington, DC 20505

Art McGarr
U.S. Geological Survey, MS-977
345 Middlefield Road
Menlo Park, CA 94025

Mr. Jack Rachlin
U.S. Geological Survey
Geology, Rm 3 C136
Mail Stop 928 National Center
Reston, VA 22092

Richard Morrow
ACDA/VI, Room 5741
320 21st Street N.W
Washington, DC 20451

Dr. Robert Reinke
WL/NTESG
Kirtland AFB, NM 87117-6008

Dr. Keith K. Nakanishi
Lawrence Livermore National Laboratory
P.O. Box 808, L-205
Livermore, CA 94550

Dr. Byron Ristvet
HQ DNA, Nevada Operations Office
Attn: NVCG
P.O. Box 98539
Las Vegas, NV 89193

Dr. Carl Newton
Los Alamos National Laboratory
P.O. Box 1663
Mail Stop C335, Group ESS-3
Los Alamos, NM 87545

Dr. George Rothe
HQ AFTAC/TGR
Patrick AFB, FL 32925-6001

Dr. Kenneth H. Olsen
Los Alamos Scientific Laboratory
P.O. Box 1663
Mail Stop C335, Group ESS-3
Los Alamos, NM 87545

Dr. Michael Shore
Defense Nuclear Agency/SPSS
6801 Telegraph Road
Alexandria, VA 22310

Howard J. Patton
Lawrence Livermore National Laboratory
P.O. Box 808, L-205
Livermore, CA 94550

Donald L. Springer
Lawrence Livermore National Laboratory
P.O. Box 808, L-205
Livermore , CA 94550

Mr. Chris Paine
Office of Senator Kennedy, SR 315

United States Senate
Washington, DC 20510

Dr. Lawrence Turnbull
OSWR/NED
Central Intelligence Agency, Room 5G48
Washington, DC 20505

Colonel Jerry J. Perrizo
AFCSR/NP, Building 410
Bolling AFB
Washington, DC 20332-6448

Dr. Thomas Weaver
Los Alamos National Laboratory
P.O. Box 1663, Mail Stop C335
Los Alamos, NM 87545

J.J. Zucca
Lawrence Livermore National Laboratory
Box 808
Livermore, CA 94550

GL/SULL
Research Library
Hanscom AFB , MA 01731-5000 (2 copies)

Secretary of the Air Force (SAFRD)

Washington, DC 20330

Office of the Secretary Defense
DDR & E
Washington, DC 20330

HQ DNA
Attn: Technical Library
Washington, DC 20305

DARPA/RMO/RETRIEVAL
1400 Wilson Boulevard
Arlington, VA 22209

DARPA/RMO/Security Office
1400 Wilson Boulevard
Arlington, VA 22209

Geophysics Laboratory
Attn: XO
Hanscom AFB, MA 01731-5000

Geophysics Laboratory
Attn: LW
Hanscom AFB, MA 01731-5000

DARPA/PM
1400 Wilson Boulevard
Arlington, VA 22209

Defense Technical Information Center
Cameron Station
Alexandria, VA 22314 (5 copies)

Defense Intelligence Agency
Directorate for Scientific &
Technical Intelligence
Washington, DC 20301

AFTAC/CA
(STINFO)
Patrick AFB, FL 32925-6001

TACTEC
Battelle Memorial Institute
505 King Avenue
Columbus, OH 43201 (Final Report Only)

Mr. Charles L. Taylor
GL/LWH

Hanscom AFB, MA 01731-5000

Dr. Ramon Cabre, S.J.
Observatorio San Calixto
Casilla 5939
La Paz, Bolivia

Prof. Hans-Peter Harjes
Institute for Geophysik
Ruhr University/Bochum
P.O. Box 102148
4630 Bochum 1, FRG

Prof. Eystein Husebye
NTNF/NORSAR
P.O. Box 51
N-2007 Kjeller, NORWAY

Prof. Brian L.N. Kennett
Research School of Earth Sciences
Institute of Advanced Studies
G.P.O. Box 4
Canberra 2601, AUSTRALIA

Dr. Bernard Massinon
Societe Radiomana
27 rue Claude Bernard
75005 Paris, FRANCE (2 Copies)

Dr. Pierre Mecheler
Societe Radiomana
27 rue Claude Bernard
75005 Paris, FRANCE

Dr. Svein Mykkeltveit
NTNF/NORSAR
P.O. Box 51
N-2007 Kjeller, NORWAY

Dr. Peter Basham
Earth Physics Branch
Geological Survey of Canada
1 Observatory Crescent
Ottawa, Ontario, CANADA K1A 0Y3

Dr. Eduard Berg
Institute of Geophysics
University of Hawaii
Honolulu, HI 96822

Dr. Michel Bouchon
I.R.I.G.M.-B.P. 68
38402 St. Martin D'Heres
Cedex, FRANCE

Dr. Hilmar Bungum
NTNF/NORSAR
P.O. Box 51
N-2007 Kjeller, NORWAY

Dr. Michel Campillo
Observatoire de Grenoble
I.R.I.G.M.-B.P. 53
38041 Grenoble, FRANCE

Dr. Kin Yip Chun
Geophysics Division
Physics Department
University of Toronto
Ontario, CANADA M5S 1A7

Dr. Alan Douglas
Ministry of Defense
Blacknest, Brimpton
Reading RG7-4RS, UNITED KINGDOM

Dr. Roger Hansen
NTNF/NORSAR
P.O. Box 51
N-2007 Kjeller, NORWAY

Dr. Manfred Henger
Federal Institute for Geosciences & Nat'l Res.
Postfach 510153
D-3000 Hanover 51, FRG

Ms. Eva Johannisson
Senior Research Officer
National Defense Research Inst.
P.O. Box 27322
S-102 54 Stockholm, SWEDEN

Dr. Fekadu Kebede
Seismological Section
Box 12019
S-750 Uppsala, SWEDEN

Dr. Tormod Kvaerna
NTNF/NORSAR
P.O. Box 51
N-2007 Kjeller, NORWAY

Dr. Peter Marshal
Procurement Executive
Ministry of Defense
Blacknest, Brimpton
Reading FG7-4RS, UNITED KINGDOM

Prof. Ari Ben-Menahem
Department of Applied Mathematics
Weizman Institute of Science
Rehovot, ISRAEL 951729

Dr. Robert North
Geophysics Division
Geological Survey of Canada
1 Observatory Crescent
Ottawa, Ontario, CANADA K1A 0Y3

Dr. Frode Ringdal
NTNF/NORSAR
P.O. Box 51
N-2007 Kjeller, NORWAY

Dr. Jorg Schlittenhardt
Federal Institute for Geosciences & Nat'l Res.
Postfach 510153
D-3000 Hannover 51, FEDERAL REPUBLIC OF
GERMANY

Prof. Daniel Walker
University of Hawaii
Institute of Geophysics
Honolulu, HI 96822